

Characterisation of a $\text{LaBr}_3:\text{LaCl}_3$ Phoswich Array Using 70-230 MeV Protons

... and a cosmic muon or two

Thesis for the Degree of Master of Science in Physics and Astronomy

Mikael Mårtensson

Department of Fundamental Physics
CHALMERS UNIVERSITY OF TECHNOLOGY
Göteborg, Sweden 2013

THESIS FOR THE DEGREE OF MASTER OF SCIENCE

Characterisation of a $\text{LaBr}_3:\text{LaCl}_3$ Phoswich Array Using 70-230 MeV Protons

... and a cosmic muon or two

MIKAEL MÅRTENSSON

Examiner:

Thomas Nilsson

Supervisor:

Andreas Heinz



Department of Fundamental Physics
CHALMERS UNIVERSITY OF TECHNOLOGY
Göteborg, Sweden 2013

Characterisation of a LaBr₃:LaCl₃ Phoswich Array Using 70-230 MeV Protons
... and a muon or two
MIKAEL MÅRTENSSON

©MIKAEL MÅRTENSSON, 2013

Department of Fundamental Physics
Chalmers University of Technology
SE-412 96 Göteborg
Sweden
Telephone + 46 (0)31-772 1000

Cover: One of crystals of the LaBr₃:LaCl₃ phoswich array used as a ΔE - E detector by separating the two pulse component of the crystal using pulse-shape analysis. The figure shows proton beam energies of 90, 130, 150, and 220 MeV.

Printed by Chalmers Reproservice
Göteborg, Sweden 2013

Abstract

The study of nuclei far from stability plays an important role in our understanding of matter and the processes involved in nuclear many-body systems, nucleosynthesis, and astrophysical processes. Studying these systems demands the use of radioactive beams, often in reactions done in inverse kinematics. The Reactions with Relativistic Radioactive Beams (R^3B) experiment at the future FAIR accelerator facility will fulfil these needs.

R^3B is in need of a calorimeter for detection of in-flight emitted γ -rays and high energy light charged particles, abbreviated CALIFA, situated around the target chamber. This thesis reports on a test experiment with a possible prototype for the forward end-cap of CALIFA. The prototype consists of four $LaBr_3(Ce):LaCl_3(Ce)$ phoswich crystals, arranged in a 2×2 array, consisting of 4 cm $LaBr_3(Ce)$ and 6 cm $LaCl_3(Ce)$.

This phoswich array is characterised by using 70-230 MeV protons of well-defined energy, cosmic muons, and simulations. Integral and correlation based off-line pulse-shape analysis tools are evaluated, optimised, and used to interpret the data. In particular, the energy deposited in the $LaBr_3(Ce)$ and the energy deposited in the $LaCl_3(Ce)$ are separated from each other, and it is demonstrated that the crystals can be used as a $\Delta E-E$ detector. In addition, the event multiplicity, crystal coincidence distribution, and the energy resolution is determined for protons. Finally, it is shown that the light output of the crystals is linear with respect to energy, and that its time characteristics differs for protons and muons.

Acknowledgements

I would like to thank Thomas Nilsson for providing me the opportunity to write this thesis, and for sharing his knowledge. A special thanks to Andreas Heinz for his daily “how’s physics?” visits, and his very helpful comments during the writing of this report.

In addition, I want to thank Håkan Johansson for providing and helping me with *ggland*, Alexandre Charpy for learning me how not to “segmentation fault”, and Ronja Thies and Fredrik Strannerdahl for helping me to ROOT out some analysis issues.

I would like to thank Olof Tengblad and the people at IEM-CSIC, Madrid, for letting me stay there to work with the phoswich array, especially José Sánchez del Río for his fast replies to all my questions regarding the detector. Also, thanks to Ángel Perea Martínez, Enrique Náchter, and Guillermo Ribeiro Jiménez for their collaboration during the tests in Krakow.

Finally, thanks to the people at IFJ, Krakow, for letting us use their cyclotron, in particular Bartłomiej Szpak for organising the stay.

Contents

1	Introduction	1
1.1	FAIR and R ³ B	1
1.2	Scintillator detectors	2
1.3	The photo-multiplier	3
1.4	The CALIFA forward end-cap prototype	4
1.5	LaBr ₃ (Ce) and LaCl ₃ (Ce)	4
1.6	Wavelet noise reduction	5
2	Proton beam test	9
2.1	Detector positioning	9
2.2	DAQ and trigger logic	9
2.3	Caen V1742 sampling ADC	11
2.4	Simulations	11
3	Pulse-shape analysis and calibration	15
3.1	Baseline subtraction	15
3.2	Distinguishing LaBr ₃ (Ce) and LaCl ₃ (Ce) hits	15
3.3	Peak finding using wavelet noise reduction	15
3.4	Pulse separation - integral method	16
3.4.1	Optimising the integral limits	17
3.5	Pulse separation - correlation method	20
3.6	Energy calibration	21
3.6.1	Calibration error	22
4	Data interpretation and discussion	23
4.1	Understanding the muon spectrum	23
4.2	The phoswich as a ΔE - E detector	24
4.2.1	Nuclear reactions	24
4.2.2	Punch through	26
4.3	Multiplicity, coincidence, and add-back	27
4.4	Energy resolution	28
4.5	Detector linearity and particle identification	29
5	Summary and outlook	33
5.1	Proton beam test	33
5.2	Pulse-shape analysis and calibration	33
5.3	Data interpretation and discussion	33
	Bibliography	35
	Glossary	37

Appendix A	Table of energy resolution	39
Appendix B	Table of multiplicity, coincidence, and add-back gain	41
Appendix C	Table of calibration parameters	43

1 Introduction

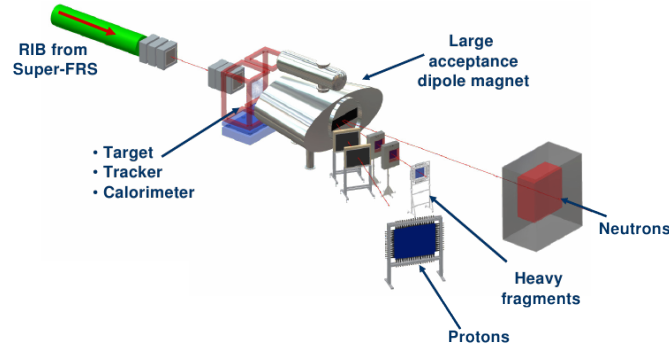
Atomic nuclei consist of protons and neutrons, which are collectively called nucleons. Nucleons are bound to each other by the nuclear force, also known as the residual strong force; the “left-over” of the strong interaction between the quarks—the building blocks of nucleons—outside the nucleon. The nuclear force acts on very small distances, about 1 fm (10^{-15} m), and quickly loses its strength beyond a few fm. For very small distances the force is highly repulsive, keeping the nucleons apart, and thus setting the size of nuclei. The force does not depend on electric charge, and as such does not discriminate between neutrons and protons. On the other hand, the Coulomb force *does* depend on electric charge, and also plays an important role in the nucleus.

A nuclear potential can be used to build an approximate model of the force between nucleons, with one potential well for neutrons, and one for protons. Neutrons and protons are fermions, and can only occupy one state each in their wells, but the proton well is not as deep for the protons, as for the neutrons, since the protons repel each other due to the Coulomb force between them. A nucleus is built by adding protons and neutron to the well. The nucleus is β -stable, i.e. it will not decay through β -decay, if the energy of the highest occupied state is equal for protons and neutrons; it is said to be proton rich, respectively neutron rich, if the energy of the highest occupied state is higher for protons, respectively neutrons. The so-called neutron drip-line is reached when the neutron potential well is filled to the brim, and no more neutrons can be added without “dripping” out of the nucleus. Likewise, there is a proton drip-line, but the Coulomb force adds an additional potential barrier that the protons have to tunnel through, making it possible for nuclei beyond the proton drip-line to exist. A nucleus with highly unbalanced proton to neutron ratio is said to have high *iso-spin*, i.e. the sum of the iso-spin projection quantum number of the nucleons is large.

The study of neutron and proton rich nuclei plays an important role in our understanding of matter and the processes involved in nuclear many-body systems, nucleosynthesis, and astrophysical processes. The testing of today’s nuclear models, and the search for a unified nuclear model, requires studying these exotic nuclei. Also, very neutron-rich nuclei are needed to study the astrophysical *r*-process; the process thought to have formed most elements of nature. In addition, a particularly interesting phenomenon called halo nuclei, where a nucleus at extreme iso-spin has a tightly bound nuclear core and loosely bound halo nucleons, has been discovered in the recent decade. Studying these systems requires the use of exotic beams and appropriate detector systems.

1.1 FAIR and R³B

The new FAIR (Facility for Antiproton and Ion Research) accelerator facility is being built at the GSI (GSI Helmholtzzentrum für Schwerionenforschung GmbH) institute in Darmstadt, Germany[8, 10]. It will be a state-of-the-art facility capable of producing a wide range of clean exotic beams. At FAIR, as a part of the NUSTAR (Nuclear Structure, Astrophysics, and Reactions) physics program, the R³B (Reactions with Relativistic Radioactive Beams) experiment will be installed at the high-energy branch of the Super-FRS (Superconducting Fragment Separator), replacing the ALADiN-LAND setup. At R³B the structure of nuclei will be probed by studying

Figure 1.1: An overview of the R³B setup.

nuclei at and beyond the drip-lines. The in-flight production method, where a radioactive beam and a target of stable nuclei is used, makes it possible to study short-lived isotopes[7].

Conventionally, nuclear reaction mechanisms are studied by direct kinematics, where a proton or neutron beam irradiates a target of heavy nuclei. With inverse kinematics, however, a heavy relativistic beam and a light, possibly thick, stable target is used. By identifying the products in-flight, measuring their momentum, and tracking them, it is possible to obtain a complete picture of the reaction that occurred.

Inverse kinematics will be used at R³B, being the only possible choice for studies of short-lived nuclei. This requires complete kinematic measurements, and puts serious demands on the detector systems; especially in the forward direction, due to the kinematic focusing of the reaction products. The R³B setup will overcome limitations of the current ALADiN-LAND setup. It will have higher magnetic rigidity, capability of detecting multi-neutron events, better momentum resolution, better energy resolution, higher efficiency, and better γ -ray detection.

The R³B setup, seen in figure 1.1, will be based on the concept of the ALADiN-LAND layout. It will have a target chamber surrounded by a calorimeter—the calorimeter for in-flight emitted γ -rays and high energy light charged particles (CALIFA)—and an optional silicon tracker. Upstream from the target there will be a set of detectors to track the incoming beam. Directly downstream from the target there will be the GSI large-acceptance dipole (GLAD) magnet to separate the reaction fragments. After the GLAD magnet the setup branches into three parts: one for protons, one for heavy fragments, and one for neutrons. The neutron branch will be dominated by the large scintillator-based New Large-Area Neutron Detector (NeuLAND). The heavy fragment branch will have diamond detectors, silicon-strip detectors, a scintillator fibre detector, channel-plate detectors, and large-area time-of-flight wall made out of organic scintillators and resistive plate chambers. The proton branch will consist of drift chambers.

1.2 Scintillator detectors

Scintillator detectors are used for a wide range of applications in nuclear physics, particle physics, medical diagnostics, energy resource exploration, and homeland security. They consist of a scintillator material and some form of light read-out device. The R³B setup will heavily depend on scintillator detectors for energy, position, and time measurements. In particular, the CALIFA detector will consist of thousands of scintillator segments.

Electrons in a scintillator material are excited by ionising radiation, and subsequently de-excite, releasing the energy absorbed by emitting photons. There are several properties to

consider when choosing a scintillator for a specific task: the density of the material, radiation hardness, light yield, signal rise and decay time, possible internal radioactivity, and cost. For example, if good energy resolution is needed and high count rates are expected, a scintillator with high light yield and short decay time should be selected.

There are four main categories of scintillators: organic, inorganic, gaseous, and glass. The organic scintillators can either be crystals, liquids, or plastics, and they scintillate through transitions involving free valence electrons in the aromatic hydrocarbon. Inorganic scintillators are usually impurity-activated alkali halides like NaI(Tl) and CsI(Tl), but doped rare earth salts like LaBr₃(Ce) and LaCl₃(Ce) are becoming more common. They scintillate through transitions in their electronic band structure. Some inorganic scintillators, e.g. NaI and LaBr₃, are very hygroscopic, and need careful wrapping. Gaseous scintillators usually consist of noble gases. The glass scintillators are very robust materials, made from lithium or boron silicates doped with cerium.

Scintillators are not necessarily linear with respect to the detected energy; in particular, the light output pulse shape can be different for different particle species, usually having a slow and a fast decay component. This is because de-excitation of different electronic states can exhibit different light output characteristics, and excited states are populated in different proportions for different energy loss per unit length, dE/dx ; the energy loss being highly dependent on particle type. This non-linearity makes it possible to distinguish different particles by performing pulse-shape discrimination (PSD) analysis, and identifying the particle type by the difference in ratio of the slow and fast components.

The total light output can also be non-linear. Scintillators can be subject to quenching, i.e. radiation-less de-excitations, or over-occupied electronic states, especially when particles deposit a lot of energy in a short distance.

1.3 The photo-multiplier

A common type of light read-out device used in scintillator detectors is the Photo-Multiplier (PM) tube. In principle a PM consists of a photo-cathode, an electron focusing system, a set of dynodes (called a dynode string), and an anode. High voltage is applied between the cathode and the anode. A photon striking the photo-cathode liberates electrons through the photo-electric effect. The electrons are focused on to the first dynode, releasing a cascade of secondary electrons. This process is repeated along the dynode string until the electrons are collected by the anode, producing an output current.

If the PM is operated correctly, i.e. at a sufficiently high voltage and within a certain range of current, it acts as a good linear amplifier. The Quantum Efficiency (QE) is the main property of the PM, and it is defined as the ratio of the number photons impinging on the photo-cathode to the number of photo-electrons released. The QE is dependent on the wavelength of the incoming light.

The two main sources of noise in a PM are statistical noise and dark current. The statistical noise of a constantly illuminated PM is often assumed to follow a Poisson distribution[13]. The noise has a multiplicative component, due to the multiplicative nature of the PM amplifier. This contribution may have a significant impact on pulse-shape analysis, as discussed in section 3.4.1.

A PM will have a non-zero decay time which potentially can smear the pulse shapes of a scintillator light response. This is good to have in mind when dealing with fast scintillator detectors.

1.4 The CALIFA forward end-cap prototype

As previously mentioned, the CALIFA detector is the calorimeter for in-flight detection of γ -rays and high energy light charged particles, that is being developed for R³B. Not only will it be able to measure individual energies, multiplicity, and sum energy of γ -rays, but also to determine the energy of high-energy light charged particles, e.g. protons, of up to 300 MeV. Furthermore, it will be able to detect neutrons that undergo nuclear reactions in the detector. CALIFA will surround the target and consists of two principle parts: the barrel and the forward end-cap. The barrel design is largely finalised, and the barrel will be composed of 1952 segments of square pyramidal frustum shaped CsI(Ti) scintillators, with large area avalanche photo diodes (LAAPDs) as read-out devices [2]. The forward end-cap will also be a highly segmented scintillator detector, but the design is not completed.

The CALIFA detector is going to replace the Crystal Ball (XB) detector used in the ALADiN-LAND setup—the predecessor of R³B. CALIFA will have higher granularity and will be able to detect γ -rays in the 100 keV to 30 MeV energy range with better resolution than the XB. It will also provide better suppression of the low energy background radiation.

The proposed design of the CALIFA end-cap consists of 750 LaBr₃:LaCl₃ phoswich (phosphor sandwich) crystals shaped as truncated isosceles trapezoid pyramids, with 4 cm of LaBr₃ and 6 cm of LaCl₃. The crystals are arranged in a semi-spherical shell, with a hole for the beam in the forward direction. The inner crystals are larger than the outer ones to keep the energy resolution of γ -rays constant in spite of Doppler broadening (see chapter 2 in the CALIFA technical design report [2]); a problem arising when reconstructing the particle rest frame energy of γ -rays emitted by sources moving with relativistic speed.

A prototype candidate for the forward end cap is currently under evaluation, and it is this prototype that will be discussed in this thesis. Figure 1.2 shows a drawing of the prototype, including crystals, casing, PM tubes, and a Double-Sided Silicon Strip Detector (DSSSD) used to obtain position data during the proton beam tests performed as a part of this thesis. There are four crystals, each with the dimensions $27 \times 27 \times 100$ mm, consisting of 40 mm of LaBr₃(Ce) (Saint Gobain BrillanCe380 [19]) in the front, and 60 mm of LaCl₃(Ce) (Saint Gobain BrillanCe350 [18]) in the back. This type of scintillator detector, composed of two optically coupled scintillator materials, is called a phoswich detector. The phoswich design, in combination with pulse-shape analysis (PSA), makes it possible to use the detector as a ΔE - E detector, and, as such, to determine the energy of the stopped particles, and also the type of the particle detected, e.g. protons, γ -rays, and even neutrons. Furthermore, the ΔE - E interpretation also makes it possible to detect and measure the energy of particles that punch through the detector. Hamamatsu R830 PM tubes are coupled to the LaCl₃ with optical grease, and are used to collect the scintillator light.

1.5 LaBr₃(Ce) and LaCl₃(Ce)

Lanthanum bromide and lanthanum chloride, both doped with cerium, are used in the phoswich detector which is the subject of this thesis. They are two relatively new scintillator materials that have emerged for commercial use during the last decade. They both have good energy resolution, high light yield, linear energy response, short rise-time, fast decay time, and low internal radioactivity (less than 1 Bq/cm³ [20]). The fast time response allows for high count rates. The main drawback is the scintillator's extreme hygroscopicity, which potentially makes packaging difficult.

The two scintillating materials used in a phoswich detector must be compatible in the sense that the scintillator in contact with the PM tube is transparent to the light emitted by the other.

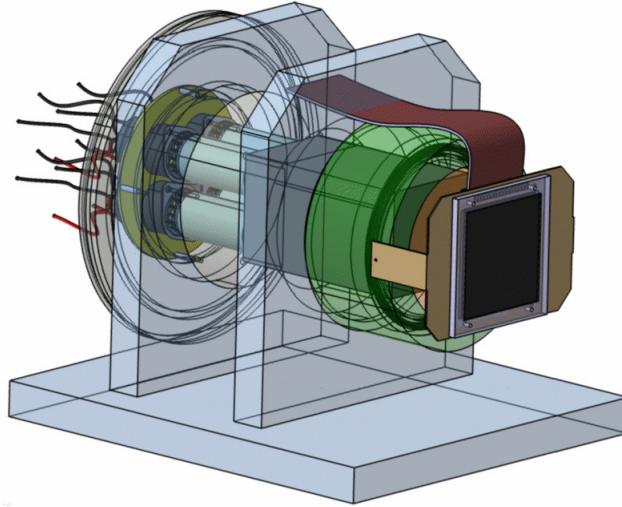


Figure 1.2: Drawing of the CALIFA $\text{LaBr}_3:\text{LaCl}_3$ phoswich prototype, with PM tubes in the back, the rectangular crystal casing in the middle, and, in the front, the DSSSD used for the proton beam tests in this work. Courtesy of J. Sánchez, Física Nuclear Experimental, IEM-CSIC, Madrid, Spain.

Scintillator	Yield (photons/keV)	Density (g/cm^3)	Decay time (ns)
$\text{LaCl}_3(\text{Ce})$	49	3.85	28
$\text{LaBr}_3(\text{Ce})$	63	5.08	16

Table 1.1: Properties of the scintillator materials used in the phoswich detector.

The second layer scintillator used in the phoswich, lanthanum chloride, is transparent to light emitted from lanthanum bromide. Furthermore, lanthanum bromide and lanthanum chloride have peak light outputs of 380 nm and 350 nm respectively, which makes them suitable for use with standard borosilicate glass plate PMs [19, 18].

The light yield, density, and decay time of each of the the two materials is presented in table 1.1. Due to the slightly different characteristics they produce light pulses with different shapes when hit by a particle, as seen in figure 1.3.

1.6 Wavelet noise reduction

Scintillator detectors are traditionally used with analogue electronics and PSA modules, both of which have a certain frequency bandwidth. In particular, the suppression of high frequencies provide noise reduction. But if digital PSA is used, as is the case in this work, it requires the whole scintillator light pulse to be sampled, and some kind of noise reduction is often needed; enter wavelets.

The Discrete Wavelet Transformation (DWT) decomposes a signal into high-pass and low-pass parts by convoluting with small wave-like filters—hence the name wavelet—and down-sampling

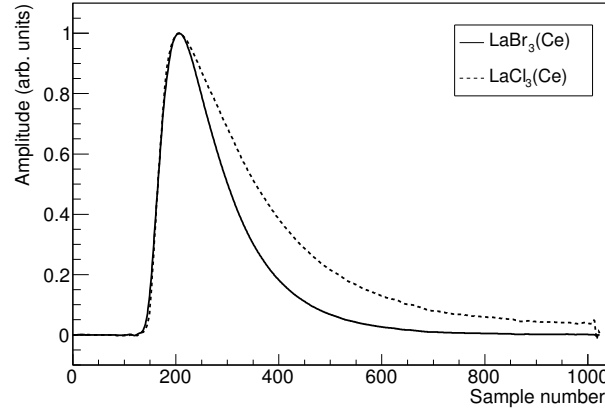


Figure 1.3: The scintillation decay time of $\text{LaBr}_3(\text{Ce})$ and $\text{LaCl}_3(\text{Ce})$ is different. The data is a normalised average of scintillator light pulse traces from a large number of muons hitting the detector.

the result, i.e. reducing the number of data points. By down-sampling the result of each filtering, the data size is kept constant. The high-pass part is called the detail, D , and the low-pass part is called the approximation, A . The approximation can then be passed through the filters again, producing second-order approximation and detail. This process can be repeated until the approximation is nothing but a single data point. Figure 1.4 shows the schematics of the DWT, and figure 1.5(a) shows a two level wavelet decomposition of a signal.

The inverse DWT works the opposite way; the approximation and details are first up-sampled, doubling their data size, by inserting a zero between each data point, then convoluted with the reconstruction wavelets h' and g' , which may be slightly different from h and g , and finally added together. For more information on wavelets see for example *a wavelet tour of signal processing* by Stéphane Mallat[14].

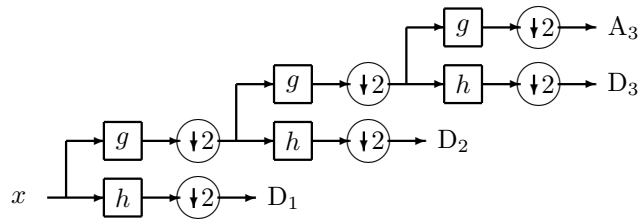


Figure 1.4: The principle of the discrete wavelet transform. The signal x is passed through the high-pass filter h and the low-pass filter g , then down-sampled. This process is then repeated for the low pass part.

The wavelet transform can be used for noise reduction of Gaussian data by making a transform of suitable level, and setting some of the detail coefficients to zero. The most robust way to determine which coefficients to set to zero is by computing the threshold, T , based on the median absolute deviation of the details and the sample size:

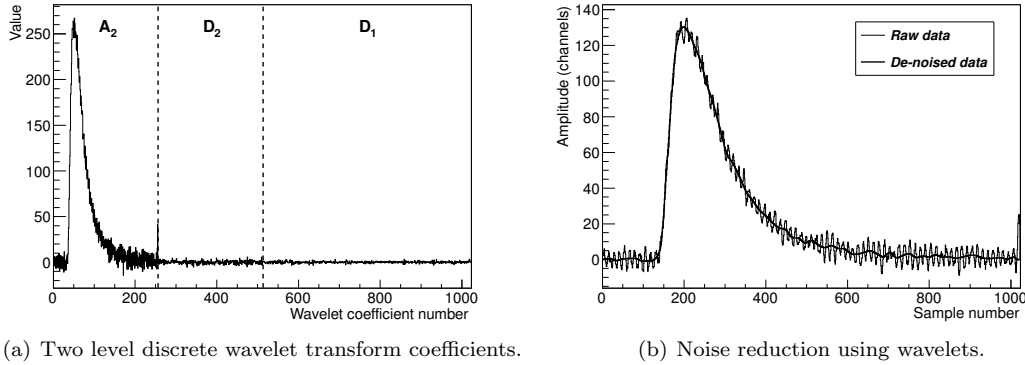


Figure 1.5: Wavelet transform of a signal from the phoswich detector, and its application for noise reduction.

$$T = \frac{\sqrt{2 \log N} \cdot \text{MAD}(x)}{0.6745} \equiv \frac{\sqrt{2 \log N} \cdot \text{median}(|D_n - \text{median}(D_n)|)}{0.6745} \quad (1.1)$$

where x is the data, N is the data sample size, D_n is the detail at level n , and 0.6745 is a normalisation factor corresponding to the one standard deviation of the Gaussian distribution. The factor $2 \log N$ was suggested by Donoho and Johnstone[6]. There are two ways of setting a threshold (thresholding): level dependent and level independent. In level dependent thresholding, T is calculated for each level n , and the details at that level are thresholded. In level independent thresholding, T is calculated from the coarsest level details D_1 , and thresholding is applied to the detail coefficient D_n of all levels. The level independent thresholding is more robust, but may not provide sufficient noise reduction.

It is also possible to do a crude noise reduction by zeroing the detail coefficients altogether. Figure 1.5(b) shows the result after setting all detail coefficients in a four level transform to zero, and reconstructing the signal.

For data affected by Poisson noise—which is the case in low-light photography and PM-tubes—thresholding by equation 1.1 does not produce good results. However, Poissonian data can be transformed to Gaussian data by the Anscombe (1948) transformation[1],

$$x_g = 2\sqrt{x_p + 3/8}, \quad (1.2)$$

where x_p is Poissonian data and x_g is the obtained Gaussian data. After treatment of the Gaussian data, it is transformed into its original form by the inverse of equation 1.2.

2 Proton beam test

This chapter describes the proton beam test of the $\text{LaBr}_3:\text{LaCl}_3$ phoswich prototype performed at the Bronowice Cyclotron Center at the Henryk Niewodniczański Institute of Nuclear Physics in Krakow, Poland, in March, 2013. The cyclotron provided proton beams at energies ranging from 70 MeV to 230 MeV.

A sampling Analogue to Digital Converter (ADC) was used to digitise the entire light pulse from the scintillator crystals. The terminology can be tricky. Here, *input(s)* or *input channel(s)* refer to the analogue inputs, i.e. of which there one for each PM, while *channel(s)* are referring to the $2^{12} = 4096$ level dynamic range of the ADC. An event trigger and its sampled pulse shape are referred to as *read-out*, *trace*, or *wave*, while the individual data points of the trace are referred to as *samples*.

2.1 Detector positioning

The beam intensity of the cyclotron was too high to use the direct beam. Instead, protons scattered off the 50 μm thick titanium foil of the beam-line exit window were used. A beam dump, consisting of a graphite block surrounded by lead at the sides and backside, was positioned approximately 3 m downstream from the exit window. The beam dump produced a rather big neutron and γ -ray radiation background at high beam energies, making it undesirable to position the detector close to it.

The detector was positioned at 1 m from the beam line exit window, at an angle of 17.8° with respect to the beam. The phoswich crystals labelled as 3 and 4 were the ones closest to the beam, for most of the experiment. Figure 2.1 shows a schematic view of the detector position in the experimental hall. There were several other detectors and equipment in the room, both upstream and downstream of the phoswich setup, but none directly in the path of the scattered protons.

2.2 DAQ and trigger logic

The data acquisition system (DAQ) used in Krakow consisted of two branches. The primary branch, presented in figure 2.2, used a Caen V1742 sampling ADC (see section 2.3) to sample the PM anodes directly from the scintillator detectors. The V1742 was running at 5 Giga-Samples per second (GS/s) and with each read-out trace consisting of 1024 samples. The output signals of the DSSSD were also sampled by the V1742 by using the summing timing filter (TF) output of the Mesytec STM-16 amplifiers, effectively reducing the 16 by 16 channels of the DSSSD to 4 by 4 channels. A computer controlled the read-out of the V1742 through an optical link using custom software. The data collected with the sampling ADC was saved for off-line pulse-shape analysis.

The secondary branch of the DAQ is seen in figure 2.3, and was based on two Caen V785 peak-sensing ADCs. The cathodes of the PMs from the scintillator detectors were fed via an amplifier chain to one of the two V785s. The DSSSD signals were amplified by a standard analogue chain and digitised by the second V785. A scaler was used to keep track of the trigger

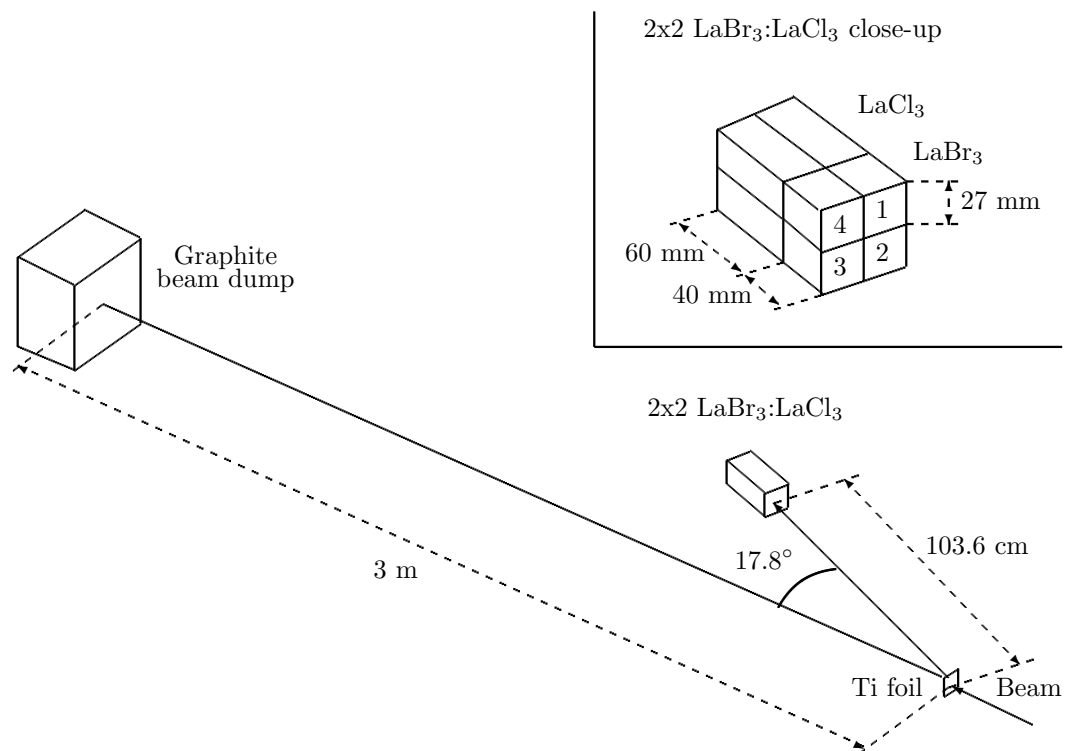


Figure 2.1: A schematic view of the detector setup during the proton beam tests in Krakow. The insert shows the geometry and orientation of the four phoswich crystals. There was also a DSSSD in front of the phoswich during the beam tests.

rates in the detectors. Two computers were used to handle the V785 branch of the DAQ: a VME 5500 in the experimental hall connected to a laptop in the control room through an Ethernet connection. This DAQ setup was mainly used to check the behaviour of the scintillators on-line, and to manage trigger rates.

Triggering of both branches of the DAQ was done by the DSSSD and, when it was added to the setup, the fifth, cylindrical $\text{LaBr}_3:\text{LaCl}_3$ phoswich. The DSSSD was used as trigger because, in contrast to the phoswiches, it is not sensitive to the γ -ray background produced by the protons hitting the graphite beam dump.

2.3 Caen V1742 sampling ADC

The Caen V1742 is a 32 input, 12 bit, 5 GS/s, sampling ADC, that uses a “domino ring sampler” to store 1024 samples of a signal. A common trigger can be provided through VME, optical link, or via the TRG-IN port. The ADC also features two fast trigger inputs, TR0 and TR1, that can be used to trigger the first and the last sixteen channels respectively. The fast triggers can be digitised with 16 bit resolution[5].

To efficiently use the ADC, it is important to be aware of certain characteristics. Cross-talk between adjacent inputs has been observed, as seen in figure 2.4. Maybe this could be remedied with proper termination of the unused inputs.

It is important to know how the input channels behave when they are unconnected, especially their baseline shape and noise, since that knowledge can be used for calibration of the raw data. The baseline shape and noise characteristics is dependent on the individual Direct Current (DC) offset settings of the input channels. Figure 2.5 shows the histograms of the unconnected channels 4, 5, and 6 plotted against each other, with channel 4 having a significantly lower DC offset setting than the channels 5 and 6. Figure 2.5(a) shows that channel 4 and 5 are badly correlated, while figure 2.5(b) shows that channel 5 and 6 are highly correlated. So, if it is desirable to use the unconnected channels for a baseline calibration, it is extremely important that they have the same DC offset setting.

2.4 Simulations

Simulations of the setup were made using Håkan Johansson’s *ggland* wrapper [11] for Geant4 [9]. The proton count rates were found for different positions of the detector, and care was taken to prevent the γ -ray background from being too high.

Also, simulations were made to get the proton energy loss in the beam exit window, DSSSD, and scintillator wrapping. Included in the simulation were: the 50 μm titanium exit window; the 500 μm silicon and $2 \times 500 \mu\text{m}$ aluminium of the DSSSD; the 500 + 1000 μm aluminium, 300 μm carbon fibre (approximated by 237 μm of 2.2 g/cm^3 carbon), and 750 μm Kapton of the phoswich wrapping[16]. The energy loss of protons in the 2 mm aluminium casing of the cylindrical phoswich was also simulated. The proton energy loss in the casing and the detected energy for both detectors can be seen in table 2.1 for a selection of beam energies.

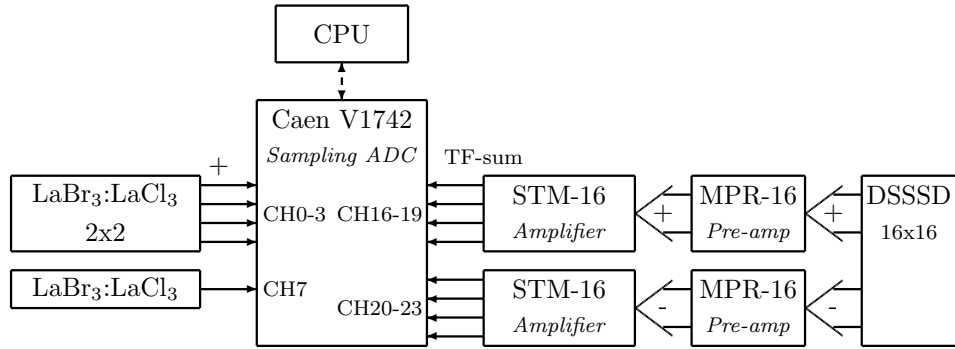


Figure 2.2: The Caen V1742 sampling ADC branch of the DAQ used in Krakow for the proton beam tests. Two $\text{LaBr}_3:\text{LaCl}_3$ phoswich detectors were used in the setup: the 2x2 crystal array and a single cylindrical crystal. The cylindrical one has 30 mm of LaBr_3 , and 50 mm of LaCl_3 ; both 20 mm in diameter. Summing timing-filter outputs of the STM-16 were used to bin together adjacent DSSSD-channels in groups of four. Solid lines show analogue signals and dashed lines show digital interfaces.

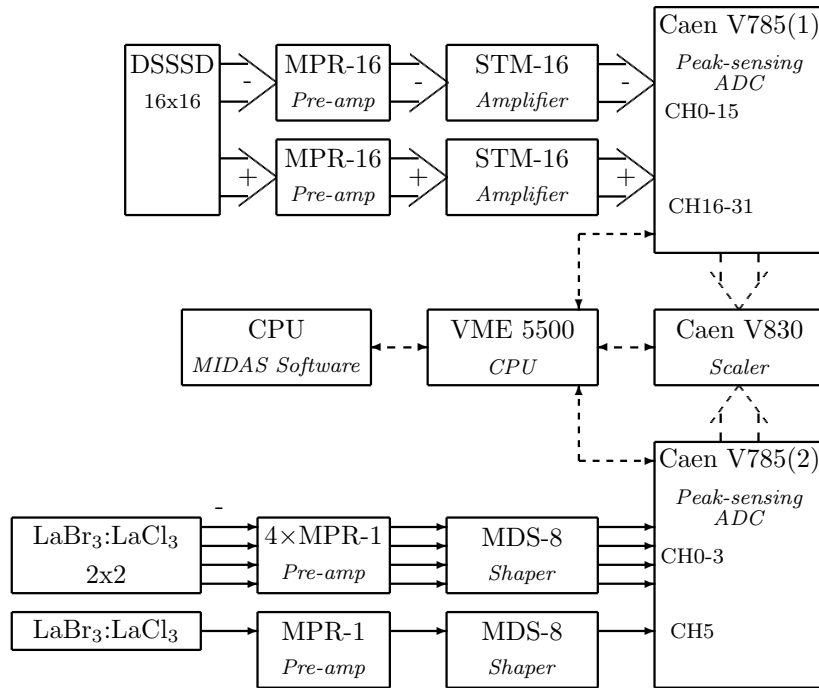


Figure 2.3: The Caen V785 peak-sensing ADC branch of the DAQ used in Krakow for the proton beam tests. Two $\text{LaBr}_3:\text{LaCl}_3$ phoswich detectors were used in the setup: the 2x2 crystal array and a single cylindrical crystal. The cylindrical one has 30 mm of LaBr_3 , and 50 mm of LaCl_3 ; both 20 mm in diameter. Solid lines show analogue signals and dashed lines show digital interfaces.

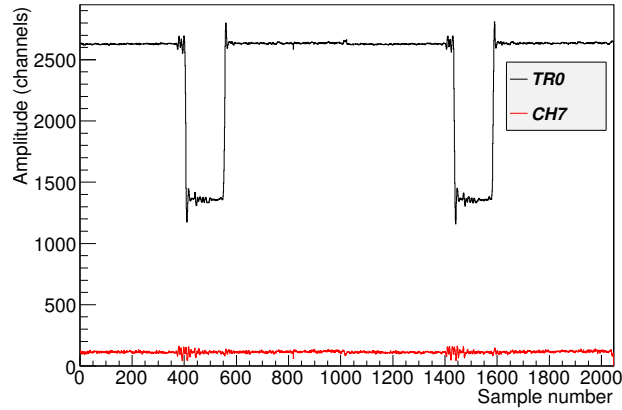


Figure 2.4: Two consecutive read-outs of two input channels of the Caen V1742 sampling ADC. TR0 is the fast trigger for input channels CH0-15. There is clearly cross-talk between the inputs; TR0 affects CH7 during its the high-frequency transitions around sample numbers 400 and 1400.

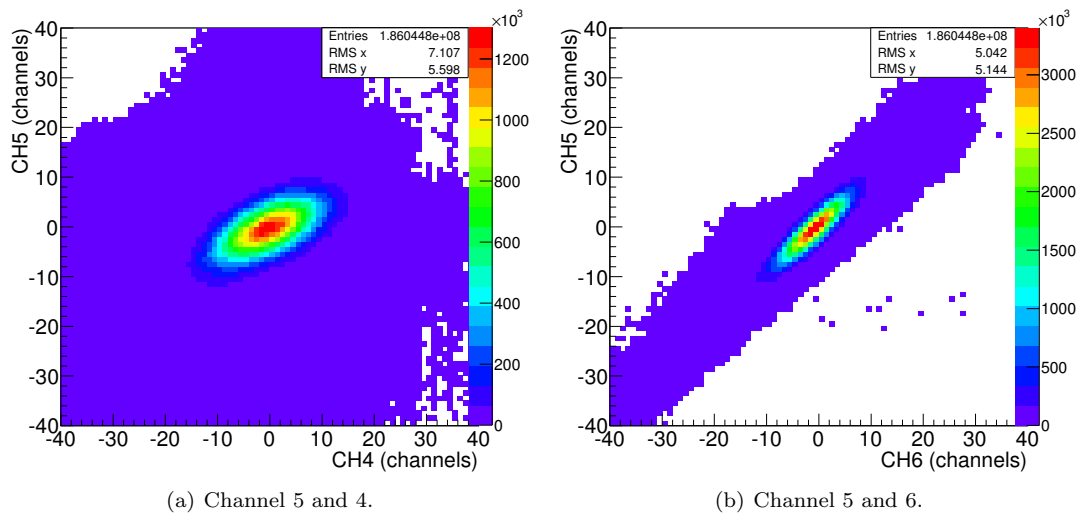


Figure 2.5: Histogram of a large number of read-outs of empty input channels 4, 5 and 6. Channel number 4 has a much lower DC offset setting than channels 5 and 6. The axes shows the deviation from the mean value of the input channel. Channel number 6 and 5 are significantly more correlated than channel 5 and 4.

Proton Beam	Energy (MeV)			
	Phoswich array		Phoswich cylinder	
	Loss	Detected	Loss	Detected
60.0	10.3	49.7	6.0	54.0
70.0	9.0	61.0	5.2	64.8
80.0	8.0	72.0	4.8	75.2
90.0	7.2	82.8	4.4	85.6
100.0	6.6	93.4	3.9	96.1
110.0	6.2	103.8	3.7	106.3
120.0	5.8	114.2	3.4	116.6
130.0	5.5	124.5	3.2	126.8
140.0	5.2	134.8	3.1	136.9
150.0	5.0	145.0	2.9	147.1
160.0	4.7	155.3	2.8	157.2
170.0	4.5	165.5	2.6	167.4
180.0	4.4	175.6	2.4	177.6
190.0	4.2	185.8	2.4	187.6
200.0	3.9	196.1	2.4	197.6

Table 2.1: Simulated energy loss in the Krakow experimental setup.

3 Pulse-shape analysis and calibration

This chapter treats the calibration of the data, the pulse-shape analysis methods, and energy calibration for the $\text{LaBr}_3:\text{LaCl}_3$ phoswich. A baseline subtraction procedure based on sampling unused inputs of the sampling ADC is proposed, a peak-finding algorithm using wavelet noise reduction is presented, and pulse-shape discrimination techniques using pulse integrals and correlation pattern recognition are discussed. Finally, an energy calibration of the detector will be presented.

3.1 Baseline subtraction

Figure 3.1(a) shows raw data from a proton depositing energy in two of the phoswich crystals; the proton deposits energy in LaBr_3 and LaCl_3 of crystal 3, and then scatters into the LaCl_3 of crystal 2. The data has a DC offset as well as a non-linear baseline component; the latter possibly due to ground-loop noise, or internal electronic characteristics of the ADC. Managing the baseline by making sure the electronic setup is sound, and by data processing, is a necessity. Having an unpredictable baseline makes it impossible to perform pulse-shape analysis and to determine the particle energy.

Luckily, all input channels in the same group of the ADC exhibit the same baseline behaviour, which makes it possible to utilise unused input channels for baseline measurement. Ideally, the baseline would be found by averaging over many unused input channels to reduce noise; however, doing so might be impractical due to the amount of disc space needed, or due to the input channels being occupied. Figure 3.1(b) shows the result after a baseline computed as the mean from three unused input channels has been subtracted from the raw data.

3.2 Distinguishing $\text{LaBr}_3(\text{Ce})$ and $\text{LaCl}_3(\text{Ce})$ hits

Due to the properties of the materials used, described in section 1.5, the pulse from a particle hitting the LaCl_3 has, assuming all other parameters to be equal, a longer tail and a smaller amplitude, compared with that of a hit in the LaBr_3 . This opens up two possibilities for distinguishing events in the detector: plotting the integral of the pulse tail, I_{tail} , versus its total integral, I_{total} , or plotting the pulse amplitude versus the total integral. These two methods will be referred to as the *integral method* and the *amplitude method* in this thesis. Figures 3.2(a) and 3.2(b) show the two methods applied to the data from the proton beam test.

The integral method is implemented by taking the integral—or rather sum, since the data is discrete—of the whole pulse, and comparing it with the integral of a part of the pulse tail. This is discussed in sections 3.4. Another approach is to use pattern recognition algorithms to separate pulse components, as discussed in section 3.5. This is referred to as the *correlation method*.

3.3 Peak finding using wavelet noise reduction

The pulse-shape analysis methods need the peak position of the sampled pulse from the scintillators. There are a number of ways to find a peak in data, including the use of the derivative.

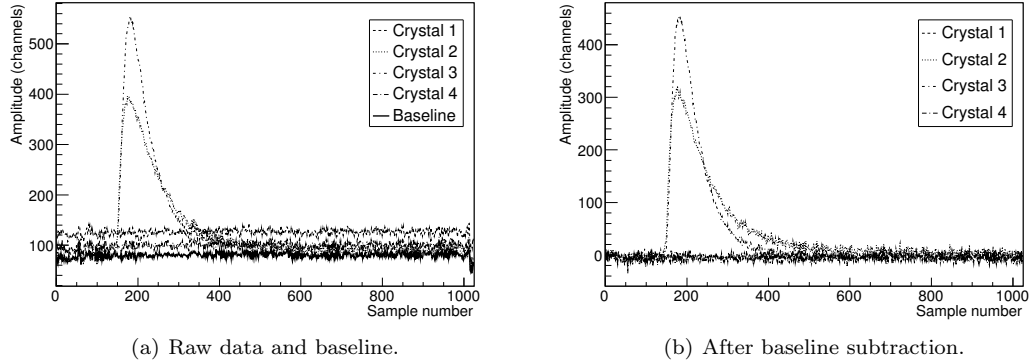


Figure 3.1: Baseline subtraction of raw data from the proton beam tests. The baseline (the lowermost curve in (a)) is estimated by taking the mean of 3 unused input channels from the same group as the input signals of the ADC.

In the case of the digitised scintillator pulses, there is only one peak, and it is sufficient to find the position of the data-point with the largest amplitude. However, the data might be too noisy to use directly.

Figure 1.5(b) shows a digitised pulse, where the peak is dominated by noise. Also shown in the same figure is the data after a crude noise reduction has been performed by taking the 4th order DWT and zeroing the detail coefficient. The shape of the pulse is preserved, and the peak is easily found by simply searching for the largest data value. Of course, the peak amplitude can also be obtained in the same way.

3.4 Pulse separation - integral method

Plotting I_{tail} versus I_{total} , as in figure 3.2(a), it is clear that the tail integral is linearly dependent on the total integral when the LaBr_3 and LaCl_3 pulse components are considered separately. The components can be described by

$$\begin{aligned} I_{tail,Br} &= a_{Br} I_{total,Br} , \\ I_{tail,Cl} &= a_{Cl} I_{total,Cl} , \end{aligned} \quad (3.1)$$

where a_{Br} and a_{Cl} are the proportionality constants. The subscripts Br and Cl indicate LaBr_3 and LaCl_3 respectively. The proportionality constants are determined by the slope of the lower and upper-left branches in the I_{tail} versus I_{total} plot, corresponding to pure energy depositions in LaBr_3 and LaCl_3 respectively, as shown in figure 3.2(a).

If the crystal total light output and pulse shape is linear with energy—which indeed is claimed by the manufacturer [17], and supported by experimental data—the tail and total integrals are linear combinations of the individual components:

$$\begin{cases} I_{total} = I_{total,Br} + I_{total,Cl} \\ I_{tail} = I_{tail,Br} + I_{tail,Cl} = a_{Br} I_{total,Br} + a_{Cl} I_{total,Cl} \end{cases} . \quad (3.2)$$

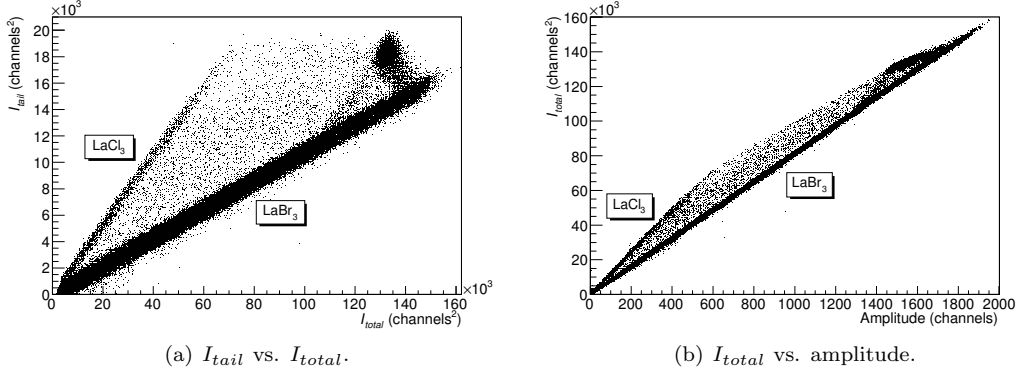


Figure 3.2: The integral (left), and the amplitude (right) method of separating the pulse components in the phoswich. The data is from a 150 MeV proton run during the Krakow beam tests.

The set of equations 3.2 can be solved for the two individual components [3]:

$$\begin{cases} I_{total,Br} = \frac{I_{tail} - a_{Cl}I_{total}}{a_{Br} - a_{Cl}} \\ I_{total,Cl} = \frac{a_{Br}I_{total} - I_{tail}}{a_{Br} - a_{Cl}} \end{cases} \quad (3.3)$$

The individual integrals are used to reconstruct the energy deposited, as described in section 3.6.

3.4.1 Optimising the integral limits

The tail, total, and nose integrals are defined as

$$I_{total} = \int_{x_0}^{x_2} f(x) dx, \quad (3.4)$$

$$I_{tail} = \int_{x_1}^{x_2} f(x) dx, \quad (3.5)$$

$$I_{nose} = \int_{x_0}^{x_p} f(x) dx, \quad (3.6)$$

where the points x_0 , x_p , x_1 , and x_2 are the start, peak, tail start, and stop of the integral, illustrated in figure 3.3(a). The peak is found by the method described in section 3.3. The remaining integral limits need to be defined in a physically sound way in order to reconstruct the energy deposited and to minimise the impact of noise.

The start of the integral, point x_0 , is the easiest one to define. It is determined by the rise time of the scintillator material and the response of the PM.

The definition of the lower and upper limits, x_1 and x_2 , is trickier, since they have a significant impact on the noise of the energy spectrum. In case of the upper limit, x_2 , it also needs to be chosen sufficiently large to correctly compute the energy. Now, consider the peak width of the I_{tail} spectrum for protons with a well-defined energy, e.g. the 150 MeV protons in the distinct

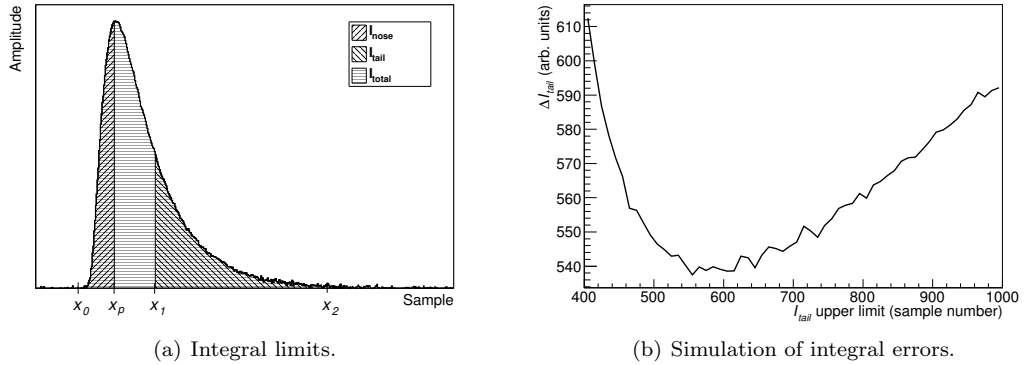


Figure 3.3: The tail integral upper limit has a clear optimum value. Figure (a) illustrates the definition of the integral limits. Figure (b) shows a simulation of the integral error for a pulse with multiplicative noise; it has been obtained by modelling the pulses with a Landau distribution plus additive and multiplicative Gaussian noise.

spot in the upper right of figure 3.2(a). If assuming a Gaussian distribution of the peak in the I_{tail} spectrum, the peak resolution is proportional to the standard deviation, $\sigma_{I_{tail}}$, divided by the mean, $\langle I_{tail} \rangle$, of the Gaussian. If the noise is purely additive, the standard deviation depends linearly on x_2 , and x_2 should be chosen as small as possible. However, if there is a multiplicative noise component, there is a value for x_2 that minimises the noise; this is illustrated in figure 3.3(b). A multiplicative noise component can be explained by the amplifier chain of the PM, as discussed in section 1.3.

Data from a 150 MeV proton beam test was chosen as basis for the optimisation, and $\sigma_{tail}/\langle I_{tail} \rangle$ was computed for a range of integral limits. Figure 3.4 shows the result. The variation in the $\sigma_{tail}/\langle I_{tail} \rangle$ between the different crystals is not surprising; the crystals all have individual impurities, defects in optical coupling, and PM characteristics. The tail integral resolution was chosen as optimisation criterion because of the impact it has on the error of the energy calibration, which is explained in section 3.6.1.

It is clear that choosing x_1 at the peak produces the smallest $\sigma_{tail}/\langle I_{tail} \rangle$. However, then the difference between the proportionality constants a_{Br} and a_{Cl} of equations 3.3 is small, and this turns out to have a severe impact on the energy resolution, as shown later in section 3.6.1. Choosing x_1 at 25 samples seems like a good compromise; there is no severe impact on resolution, and the pulse components should be well separated. The best choice for x_2 , given a choice of x_1 at 25 samples, is between 200 and 250, depending on the crystal. However, this optimisation is based on 150 MeV proton data, and the traces with the longest tails are produced just below the detector punch through limit, at about 200 MeV; choosing a slightly larger x_2 , say 300, will ensure that there is no significant truncation of the tail integral.

Empirically, it had been determined that choosing $x_1 = 100$ samples right of the peak, and $x_2 = 300$ samples right of the peak produces the best resolution in the energy spectrum—provided that the Caen V1742 ADC is running at 5 GS/s and 1024 point sample size.

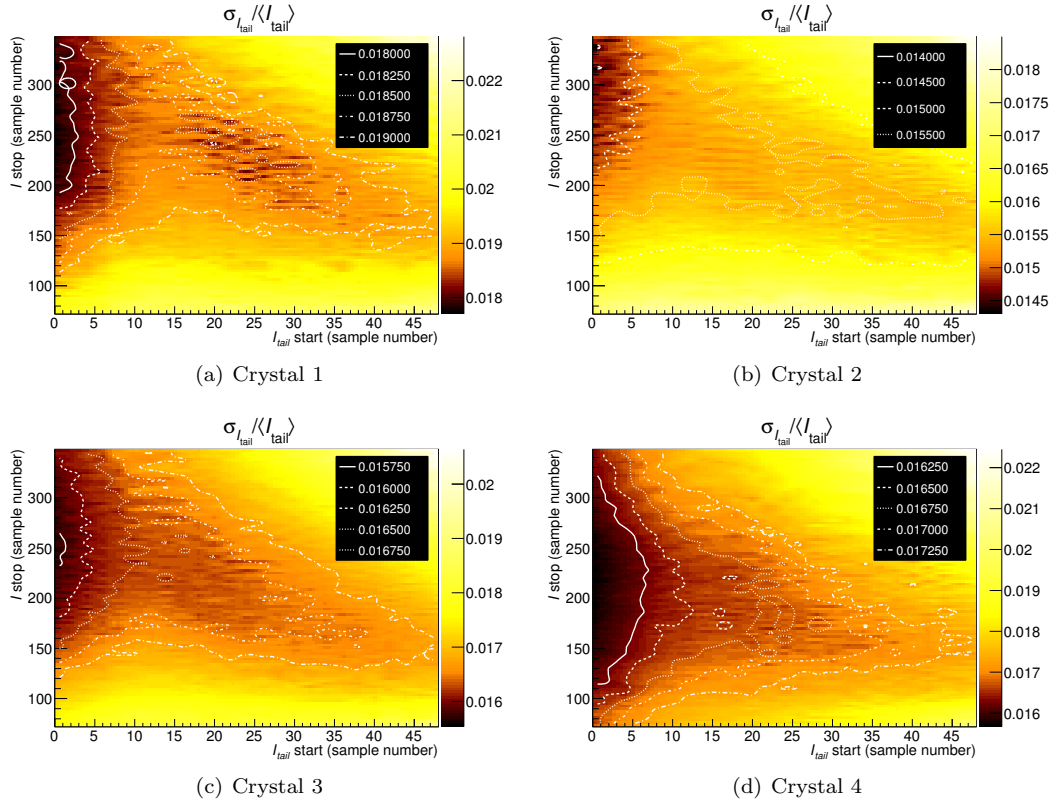


Figure 3.4: Optimisation of tail integral limits by minimising the standard deviation divided by the mean of a Gaussian fit to the I_{tail} spectrum of 150 MeV protons for the four crystals used in the experiment.

3.5 Pulse separation - correlation method

The light pulse produced from a particle hitting the phoswich detector is a superposition of two components: one from LaBr_3 and one from LaCl_3 . Consequently, an individual pulse separation can be performed by comparing the digitised traces to a mix of the LaBr_3 and LaCl_3 templates traces. The templates have to be computed by averaging traces from hits where it is known that the particle only hit one of the scintillator materials.

A trace is decomposed by normalising its amplitude, and computing the correlation between the recorded pulse and a mixture of the two templates. A prerequisite to be able to use normalised templates is that the total integral of the pulse is directly proportional to the amplitude, which indeed seems to be the case, as seen in figure 3.2(b). The pulse separation is simply

$$f = (1 - x) \cdot f_{\text{LaBr}_3} + x \cdot f_{\text{LaCl}_3} ,$$

where f is the decomposed/recomposed pulse, f_{LaBr_3} is the LaBr_3 template, f_{LaCl_3} is the LaCl_3 template, and x is the percentage of f_{LaCl_3} . The fraction x is determined by sweeping x from 0 to 1 and saving the x for which f has the highest correlation with the original data; a better way would be using more refined search algorithms for x . The correlation is given by the *sample Pearson correlation coefficient*:

$$r = \frac{\sum_{i=1}^n (X_i - \bar{X})(Y_i - \bar{Y})}{\sqrt{\sum_{i=1}^n (X_i - \bar{X})^2} \sqrt{\sum_{i=1}^n (Y_i - \bar{Y})^2}} , \quad (3.7)$$

where X and Y are the trace and template data series, respectively.

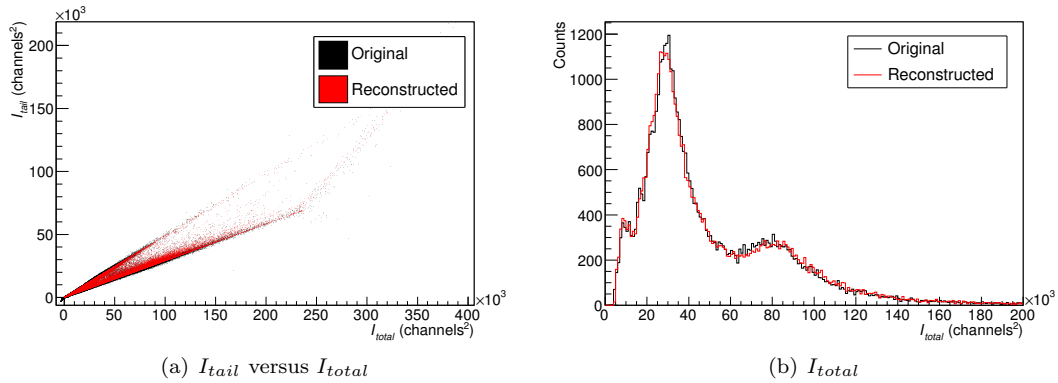


Figure 3.5: Decomposition of traces in their LaBr_3 part and their LaCl_3 part, by using correlation pattern recognition, and putting it back together. The data displayed show the energy deposited by cosmic muons in detector 1, while requiring a coincidence with detector 2.

After separating the I_{total} components, the bromide and chloride integrals are given by

$$\begin{cases} I_{total,Br} = xAI_{total} \\ I_{total,Cl} = (1 - x)AI_{total} \end{cases} ,$$

where A is the amplitude of the original trace. Figure 3.5 shows the result of decomposing and reconstructing the traces from muons. The individual integrals are used to reconstruct the energy deposited, as described in section 3.6.

3.6 Energy calibration

The energy deposited in the LaBr_3 , ΔE_{Br} , and the energy deposited in the LaCl_3 , ΔE_{Cl} , can be extracted from the separated pulse integrals (see sections 3.4 and 3.5) by a linear calibration:

$$\begin{aligned}\Delta E_{\text{Br}} &= b_0 + b_1 I_{\text{Br}}, \\ \Delta E_{\text{Cl}} &= b_2 + b_3 I_{\text{Cl}},\end{aligned}\tag{3.8}$$

where b_0 and b_1 have to be determined by a linear fit to known energy depositions in the LaBr_3 branch of the I_{tail} versus I_{total} spectrum; likewise, the LaCl_3 calibration parameters b_2 and b_3 can be determined by a linear fit to known energy depositions in the LaCl_3 . The offset terms b_0 and b_2 are generally non-zero, because of properties of the read-out electronics, errors in the baseline subtraction, and uncertainties of the calibration energies.

The energy calibration of the proton beam tests in Krakow is based on known cyclotron beam energies, and simulated energy loss (table 2.1) in the exit window and detector casing (see section 2.4). The LaBr_3 calibration parameters were found directly by fitting the $I_{\text{total,Br}}$ for 70, 80, 90, 100, 110, 120, and 130 MeV runs; energies completely stopped in the LaBr_3 . After finding the LaBr_3 calibration parameters, the LaCl_3 parameters can be computed using protons that are stopped in the LaCl_3 . The energy deposited in the LaCl_3 is found by subtracting the energy deposited in the LaBr_3 from the total energy. Proton beam energies of 140, 150, 160, 170, and 180 MeV were used to compute the LaCl_3 calibration parameters.

Another calibration source is the energy deposited by cosmic muons. Muons possess many good qualities: they are readily available, they are free, and—since they are minimum ionising particles—their energy deposition is rather well-defined. With the particular geometry of the four-crystal prototype it is possible to obtain two distinct peaks in the I_{total} spectrum by requiring a coincidence between detectors to define the amount material traversed by the muon. One of the peaks originates from pure hits in the LaBr_3 and one is caused by pure hits in the LaCl_3 . That makes it possible to perform a two point calibration, i.e. to get the b_1 and b_2 parameters of the energy calibration in equation 3.8. It is also possible to get a third calibration point, provided enough statistics from muons traversing the whole length of the crystal is available. With the geometrical complexities of the CALIFA end-cap design, it will be possible to make several different coincidence requirements, as such defining a number of muon traces, and obtaining more energy calibration points.

A drawback of using muons for energy calibration is that the energy deposited from the muons needs to be known, either from simulations, or preferably from comparison with measurements of a well-defined beam. Luckily, this only needs to be done once. Muon data can be collected between beam times, during the so called “off-spill” periods in the experiment, or indeed any other time. A potential limitation is the low count-rates of cosmic muons: approximately one muon per square centimetre and minute.

3.6.1 Calibration error

The total energy calibration can be written

$$\begin{cases} \Delta E_{\text{Br}} &= b_0 + b_1 I_{\text{total,Br}} = b_0 + b_1 \frac{I_{\text{tail}} - a_{\text{Cl}} I_{\text{total}}}{a_{\text{Br}} - a_{\text{Cl}}} \\ \Delta E_{\text{Cl}} &= b_2 + b_3 I_{\text{total,Cl}} = b_2 + b_3 \frac{a_{\text{Br}} I_{\text{total}} - I_{\text{tail}}}{a_{\text{Br}} - a_{\text{Cl}}} \end{cases}, \quad (3.9)$$

when combining equations (3.3) and (3.8). Given a function $y = f(x_1, x_2, \dots, x_n)$ the first order error propagation is

$$|\Delta y| = \sum_{i=1}^n \left| \frac{\partial f}{\partial x_i} \right| |\Delta x_i|.$$

Applying this to the calibration (3.9) for parameters $b_0, b_1, b_2, b_3, a_{\text{Br}}, a_{\text{Cl}}, I_{\text{total}}$, and I_{tail} yields

$$\begin{aligned} \Delta(\Delta E_{\text{Br}}) &= |\Delta b_0| + |I_{\text{total,Br}}| |\Delta b_1| + \left| \frac{b_1 I_{\text{total,Br}}}{a_{\text{Br}} - a_{\text{Cl}}} \right| |\Delta a_{\text{Br}}| + \left| \frac{b_1 I_{\text{total,Cl}}}{a_{\text{Br}} - a_{\text{Cl}}} \right| |\Delta a_{\text{Cl}}| \\ &\quad + \left| \frac{b_1 a_{\text{Cl}}}{a_{\text{Br}} - a_{\text{Cl}}} \right| |\Delta I_{\text{total}}| + \left| \frac{b_1}{a_{\text{Br}} - a_{\text{Cl}}} \right| |\Delta I_{\text{tail}}|, \end{aligned} \quad (3.10)$$

$$\begin{aligned} \Delta(\Delta E_{\text{Cl}}) &= |\Delta b_2| + |I_{\text{total,Cl}}| |\Delta b_3| + \left| \frac{b_3 I_{\text{total,Br}}}{a_{\text{Br}} - a_{\text{Cl}}} \right| |\Delta a_{\text{Br}}| + \left| \frac{b_3 I_{\text{total,Cl}}}{a_{\text{Br}} - a_{\text{Cl}}} \right| |\Delta a_{\text{Cl}}| \\ &\quad + \left| \frac{b_3 a_{\text{Br}}}{a_{\text{Br}} - a_{\text{Cl}}} \right| |\Delta I_{\text{total}}| + \left| \frac{b_3}{a_{\text{Br}} - a_{\text{Cl}}} \right| |\Delta I_{\text{tail}}|. \end{aligned} \quad (3.11)$$

Firstly, note that $\Delta(\Delta E_{\text{Cl}})$ is more sensitive to electronic noise in I_{total} and I_{tail} due to the fact that $b_3 \approx 2b_1$ (because of the lower light-yield of LaCl_3). Secondly, note the $1/(a_{\text{Br}} - a_{\text{Cl}})$ dependence, making a good pulse separation critical; the error grows quickly when $a_{\text{Br}} - a_{\text{Cl}}$ approaches zero. Finally, that the ΔI_{total} term contains a factor of a_{Br} or a_{Cl} , both which are in the order of 0.15, that suppresses the noise. The ΔI_{tail} terms does not have this suppressing factor, and hence it was chosen as the quantity used in optimising the tail integral (section 3.4.1). The above analysis shows that the pulse separation needs to be taken into account in the optimisation of the integral limits.

4 Data interpretation and discussion

This chapter treats the interpretation of data from the phoswich array using the pulse-shape analysis methods discussed in the previous chapter. Data from both cosmic muons and 70-230 MeV protons is considered. First, peaks in the muon energy spectrum is interpreted. Then, the detector is used in ΔE - E configuration to analyse data from the proton beam tests in Krakow, and the proton energy resolution of the detector is investigated. Finally, the linearity of the detector is discussed, and the pulse shape of the scintillator light output is shown to be different for muons and protons.

4.1 Understanding the muon spectrum

The kinetic energy loss of a particle travelling through matter is described by the Bethe-Bloch formula [13]. To leading order the energy deposition is proportional to the amount of material traversed, times the density of the material, and times the ratio of the proton number to mass number. LaBr_3 and LaCl_3 have different light output and density, as seen in table 1.1, which means that a minimum ionising particle, like the muon, produces two distinct peaks in the energy spectrum. Because of this, the expected ratio of the light output of the two crystals for a minimum ionising particle, with fixed energy, traversing a well-defined distance in a material, is described by

$$\frac{dE_{\text{LaBr}_3}}{dE_{\text{LaCl}_3}} \cdot \frac{y_{\text{LaBr}_3}}{y_{\text{LaCl}_3}} = \frac{((3Z_{\text{Br}} + Z_{\text{La}}) \cdot \rho_{\text{LaBr}_3}) / (3A_{\text{Br}} + A_{\text{La}})}{((3Z_{\text{Cl}} + Z_{\text{La}}) \cdot \rho_{\text{LaCl}_3}) / (3A_{\text{Cl}} + A_{\text{La}})} \cdot \frac{y_{\text{LaBr}_3}}{y_{\text{LaCl}_3}}, \quad (4.1)$$

where y is the light yield, and ρ is the density of the material; Z is the proton number, and A is the mass number of the elements. The material or element is indicated by a subscript.

Putting in values from table 1.1, and the correct proton and mass numbers, we find

$$\frac{dE_{\text{LaBr}_3}}{dE_{\text{LaCl}_3}} \cdot \frac{y_{\text{LaBr}_3}}{y_{\text{LaCl}_3}} \approx 2.87. \quad (4.2)$$

Table 4.1 shows the peak positions of the I_{total} spectrum from a muon run that lasted for several days, with the detector oriented horizontally. To get the peak energy position, muons hitting the LaBr_3 were separated from those hitting the LaCl_3 by isolating the two branches of the I_{tail} versus I_{total} plot. Next, the values were obtained by fitting a landau distribution and a linear background to the spectrum. The values are slightly lower than expected from the calculation. This can be due to imperfect light propagation in the interface between the two crystal materials, or—since the LaCl_3 is directly coupled to the PM tube, while the LaBr_3 is glued to the LaCl_3 —the LaCl_3 PM-tube coupling. Also, the geometry of the crystal and the PM-tube affects the peak ratio; the crystal is square while the PM-tube is circular. Another source of error is the fit itself and the difficulty to estimate the background.

Crystal	Peak position (ADC channels ²)		
	LaBr ₃	LaCl ₃	Ratio
1	79567 ± 356	29161 ± 89	2.729 ± 0.021
2	67389 ± 461	25753 ± 97	2.620 ± 0.028
3	101566 ± 461	37609 ± 123	2.701 ± 0.021
4	55774 ± 291	22061 ± 87	2.528 ± 0.023

Table 4.1: Peak positions of muon I_{total} (energy) spectra in the four LaBr₃:LaCl₃ crystals used in this work. The theoretical value (from a “back of the envelope” calculation) of the ratio is 2.87. For details see the text.

4.2 The phoswich as a ΔE - E detector

After separating the pulse components (equation 3.3 or 3.8), and making an energy calibration (equation 3.8), as described in chapter 3, the phoswich can be used as a ΔE - E detector by plotting ΔE_{Br} against $\Delta E_{Br} + \Delta E_{Cl}$. Figure 4.1 shows a ΔE - E plot of protons from the Krakow beam tests. Protons with energies lower than the punch through limit (see section 4.2.2) of the LaBr₃ deposit their full energy in the LaBr₃, e.g. the 90 and 130 MeV runs of figure 4.1. Proton with energies between the LaBr₃ punch through and the total punch through are stopped in the LaCl₃, after depositing part of their energy in the LaBr₃. For energies above the total punch through, the detector behaves as a ΔE - ΔE detector, but it is still possible to determine the energy of the incident protons.

Figure 4.2 shows data from a 220 MeV proton run. There are several distinct features in the figure, originating from different kinds of event classes inside the phoswich detector. By isolating features in one crystal, and investigating coincident events in other crystals, it is possible to determine the nature of them. The event classes labelled in figure 4.2 represent the following:

1. 220 MeV protons that have traversed the whole length of the detector.
2. Lower energy protons fully stopped in the LaCl₃.
3. Particles scattered out of the crystal.
4. Possibly nuclear reactions, see section 4.2.1.
5. Particles that deposit energy in the LaCl₃ only. They have no coincident events in other crystals, so they are most likely scattered from surrounding equipment.
6. Particles that deposit energy in the LaCl₃, most of which are scattered from other crystals. Events labelled as number 3 are the complementary events; i.e. events labelled as number 6 have corresponding events labelled number 3 in other crystals.
7. Particles depositing energy in the LaBr₃, about half of them being scattered into or out of neighbouring crystals.
8. Particles stopped in the LaBr₃.

4.2.1 Nuclear reactions

Events marked as number 4 in figure 4.2 were first suspected to originate from pile-up, but isolating those events and plotting the signal traces does not support this assumption. With

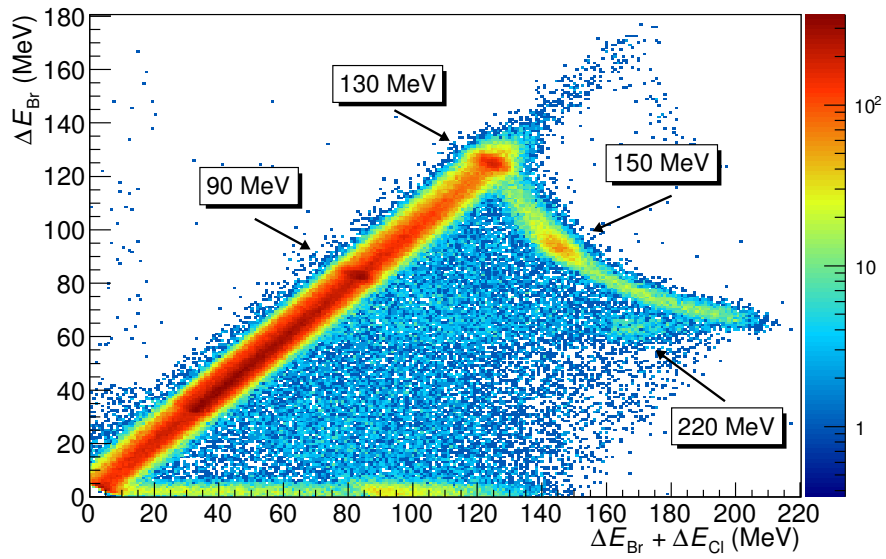


Figure 4.1: The phoswich detector used as a ΔE - E detector with data from the proton beam tests in Krakow. The beam energies (shown in the labels) are not corrected for energy losses in the detector casing.

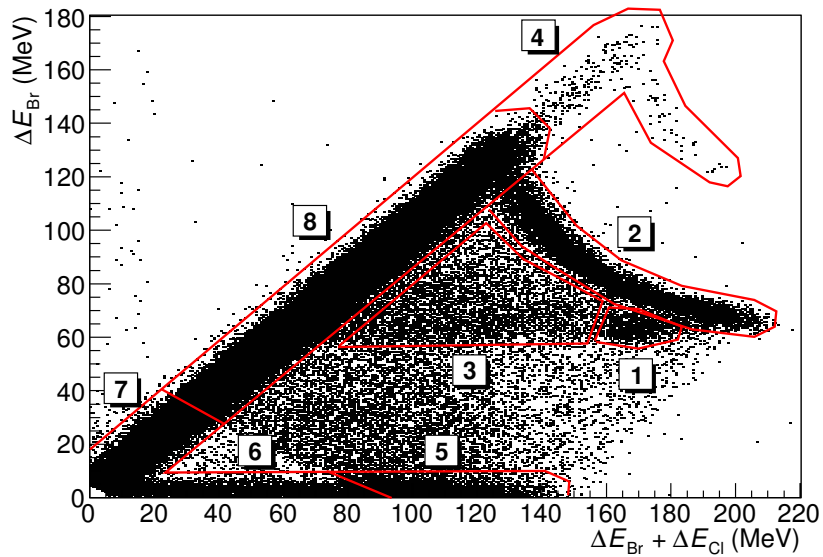


Figure 4.2: The phoswich detector used as a ΔE - E detector with data from the proton beam tests in Krakow. The beam energy was 220 MeV. The labelled features are explained in section 4.2.

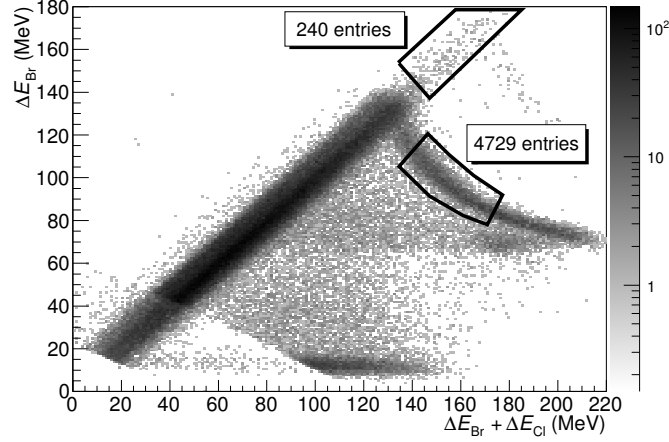


Figure 4.3: Possible nuclear reactions in the detector (top box) and fully stopped particles of the same energy.

a maximum proton flux of 10 kHz through the detector, and 1 kHz of accepted triggers—each read-out with a sample length of 204.8 ns—the chance of pile-up is in the order of 0.2%.

Could it be nuclear reactions? The probability for nuclear reactions can be estimated from the geometrical cross section, σ_r , times the number of target nuclei, n_T , seen by the beam:

$$\sigma_r = \pi(R_0^2 A_T^{2/3} + r_p), \quad (4.3)$$

$$n_T = \frac{N_A}{M_T} \rho_T l_T, \quad (4.4)$$

where $R_0 \approx 1.2$ fm [12], A_T is the target mass number, $r_p = 0.8768$ fm is the proton charge radius [15], n_T is the number of targets per unit area, N_A is Avogadro's constant, M_T is the target molar mass, ρ_T is the target density, and l_T is the target thickness. For LaBr_3 $M_T = (4 \cdot 79.9 + 138.9) \cdot 1$ g/mole, $A_T = 4 \cdot 79.9 + 138.9$, and $\rho_T = 5.08$ g/cm³ [12]. These values give $\sigma_r n \approx 2\%$ nuclear reactions. From making cuts in the graph for the last $l_T = 1$ cm of the LaBr_3 , as illustrated in figure 4.3, the measured reaction ratio is $5.1 \pm 0.4\%$. The conclusion is: yes, it is probably nuclear reactions, although the geometric reaction cross section is a simple model, and the actual cross section can differ significantly.

4.2.2 Punch through

The phoswich crystals have two punch through limits: the first one when a particle has enough energy to punch through the LaBr_3 , and the second one when it punches through the LaCl_3 as well. The first punch through energy is found by fitting the following piece-wise function to the ΔE_{Br} vs. $\Delta E_{\text{Br}} + \Delta E_{\text{Cl}}$ spectrum:

$$f(x) = \begin{cases} c_0 + x & \text{for } 0 < x < c_p \\ c_p + c_1 \left(\frac{\ln(c_2(x+1-c_p)^2)}{1-(x+1-c_p)^{-2}} - 1 \right) & \text{for } c_p < x \end{cases} \quad (4.5)$$

Detector	Energy (MeV)	
	Partial	Total
1	128.5	200
2	128.5	198
3	128.5	200
4	128.5	198
5	108.5	185

Table 4.2: Punch through limits for protons detected in the LaBr₃:LaCl₃ phoswiches. Partial punch through refers to the energy where a particle punches through the LaBr₃ but not the LaCl₃; total punch through happens when the particle punches through the LaCl₃ as well. Detectors 1 to 4 are the crystals of the 2 × 2 phoswich array, and detector 5 is the shorter crystal.

where c_p is the partial punch through limit, and c_0 , c_1 , and c_2 are fitting parameters. At energies lower than c_p the function is just a straight line, since then ΔE_{C1} is zero, but with a possible offset, c_0 , due to calibration uncertainties. At energies above the partial punch through, the curve follows the Bethe formula for the energy loss of particles in matter[12]:

$$-\frac{dE}{dx} = \frac{4\pi}{m_e c^2} \frac{nz^2}{\beta^2} \left(\frac{e^2}{4\pi\epsilon_0}\right)^2 \left[\ln\left(\frac{2m_e c^2}{I} \frac{\beta^2}{1-\beta^2}\right) - \beta^2 \right], \quad (4.6)$$

where m_e is the electron mass, c is the speed of light, $\beta = v/c$ is the velocity of the particle, n is the number density of the stopping material, z is the charge of the particle, ϵ_0 is the vacuum permittivity, and I is the mean excitation energy of the atomic electrons in the stopping material. The relationship between the particle's kinetic energy, T , and its β -factor is

$$T = m_p c^2 \left(\frac{1}{\sqrt{1-\beta^2}} - 1 \right), \quad (4.7)$$

where m_p is the proton mass. The fit function (4.5) is found by solving equation (4.7) for β , inserting it into equation (4.6), and putting $T/(m_p c^2) = x$.

The punch through limits were found to be 128.5 MeV for the partial punch through and about 199 MeV for the total punch through. For the shorter crystal, the one with 3 cm LaBr₃ and 5 cm LaCl₃, the punch through limits were found to be 108.5 and 185 MeV respectively. Table 4.2 shows the punch through limits for all the crystals.

4.3 Multiplicity, coincidence, and add-back

The multiplicity of an event is the number of detector segments that produce a signal during one trigger gate. It is desirable to have low multiplicity, since it is easier to reconstruct the detected energy for low-multiplicity events; ideally, the multiplicity is 1. For the phoswich array investigated in this thesis, the multiplicity 1 events constitute more than 90% of the total events for fully stopped protons, and more than 98% for protons stopped in the LaBr₃. Table B.1 in appendix B shows the multiplicities for protons of known kinetic energy detected by the phoswich array.

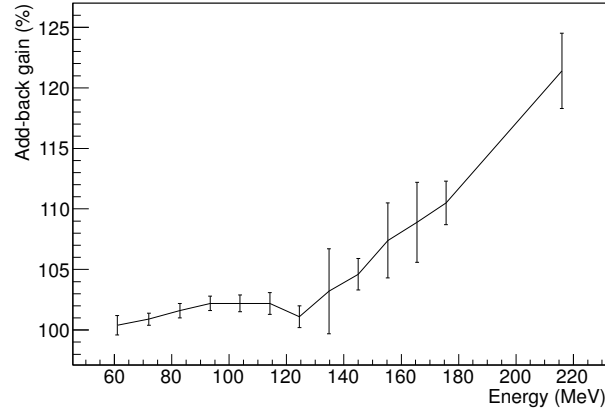


Figure 4.4: The percentage gain in statistics by using add-back for fully stopped protons, or, in case of 220 MeV, protons that have punched through the detector. The energy is the detected proton kinetic energy, i.e. the proton beam energy with the energy loss in the detector casing subtracted. The error is the propagated 1σ intrinsic statistical error of the count numbers.

An add-back routine is an algorithm that aims at reconstructing the total energy deposited in a detector by adding the energy detected in the various detector segments. It is implemented for the phoswich array by adding the energy detected in all crystals, but discarding the contribution from a particular crystal if its pulse amplitude is below a certain threshold. Figure 4.4 shows the gain of using add-back for reconstructing the full proton energy. Table B.1 shows the complete list of the number of events gained by employing add-back.

High energy protons travel a long portion of the crystal length, in comparison with low energy protons, before they are stopped. As a consequence, they are more likely to scatter out of the detector, or into a neighbouring crystal. This is why the multiplicity and the add-back gain are high at high energies.

The coincidence seen between crystal pairs has also been investigated. Expressed in percentage of total number of coincidences, it is on average: 7% and 16% for the horizontal pairs 1-2 and 3-4 respectively, 32% and 41% for the vertical pairs 1-4 and 2-3 respectively, and less than 1% for both the diagonal pairs 1-3 and 2-4 (see figure 2.1 for the crystal numbering). As expected, the percentage of coincidence in diagonal crystal pairs is low. What is surprising is the large difference in coincidences between horizontal and vertical crystal pairs; this might indicate a non-circular beam profile. See table B.2 in appendix B for the complete list, including statistical errors.

4.4 Energy resolution

The energy resolution of the ΔE_{Br} versus $\Delta E_{Br} + \Delta E_{Cl}$ plot is heavily dependent on the processing. Instead, the I_{total} spectrum was used to check the best possible energy resolution of the phoswich and DAQ combination. A linear background with a Gaussian peak was used for energies below the partial punch through; at energies above the partial punch through, the total energy deposition spot was isolated, and a Gaussian was fitted to the spectrum. Figure 4.5 shows

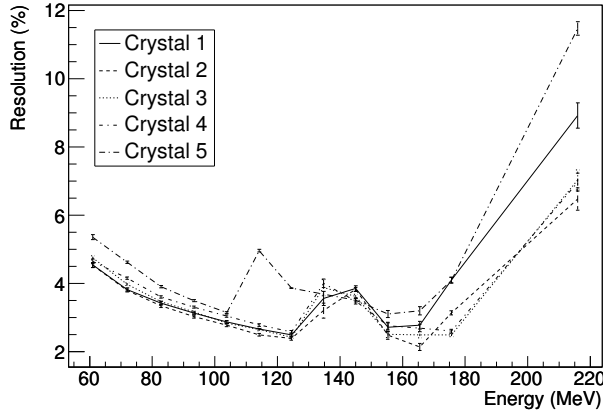


Figure 4.5: Energy resolution of the crystals, from the I_{total} spectrum. The energy is the proton kinetic energy, with correction for energy loss in the casing material. The 2σ error bars are the errors calculated from a Gaussian fit to the I_{total} spectrum.

the energy resolution, expressed in percent, calculated according to

$$\text{Resolution} = \frac{\Delta E_{FWHM}}{E} \approx 2.3548201 \times \frac{\sigma}{x_0}, \quad (4.8)$$

where σ and x_0 are the standard deviation and mean of the Gaussian fit, respectively. The energy is the cyclotron energy corrected for the simulated energy loss in the casing material. The energy dispersion of the cyclotron itself is said to be less than 0.7%. The energy resolution of the five crystals is also tabulated in appendix A.

4.5 Detector linearity and particle identification

The linearity of the detector can be validated in several ways. Figures 3.2(a) and 3.2(b), when both are considered, shows that both the tail integral and the amplitude scales linearly with the total integral for pure hits in the LaBr_3 and LaCl_3 . In figure 4.6 individual events have been isolated for a range of energies, which provide a more explicit confirmation of the linearity of the detector.

Figure 4.7 shows a comparison between traces from a 70 MeV proton and a muon depositing 70 MeV in the detector; both hitting the LaBr_3 . The muon trace has a much longer decay time. However, it should be noted that the PM voltage was not the same for the muon and the proton—it was 1000 V for the muons and 900 V for the protons—and that the voltage difference could affect the PM decay time.

A possible explanation is that different excited electronic states are populated in the crystal depending on the energy deposited per unit length, dE/dx . These states might not have the same half-life, and will produce different pulse decay times—this is exactly the process exploited in PSD algorithms using slow and fast pulse components to distinguish particle species[13]. Indeed, the high energy muon, being a minimum ionising particle, is not stopped in the crystal, and has a small dE/dx . The proton, on the other hand, is fully stopped in the crystal, and has the so-called Bragg-peak inside the crystal, i.e. it deposits a significant fraction of its total kinetic

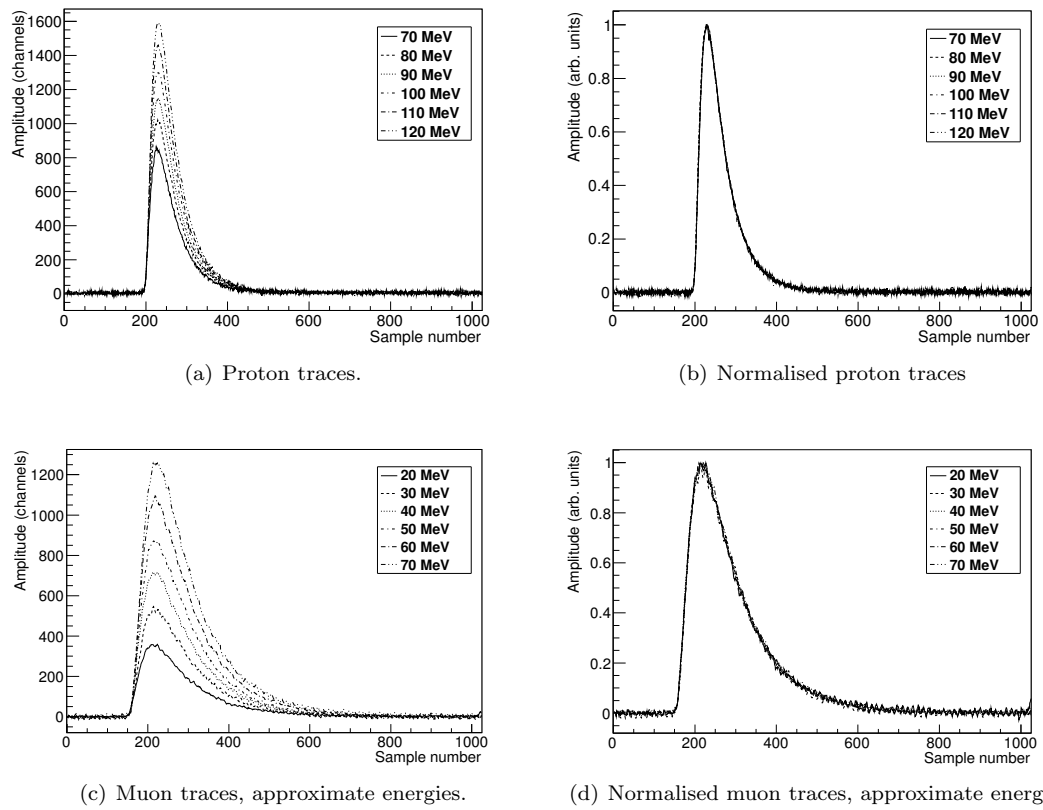


Figure 4.6: Lanthanum bromide traces from protons and muons, at different energies. The normalised traces shows that the pulse shape is preserved over a range of particle energies.

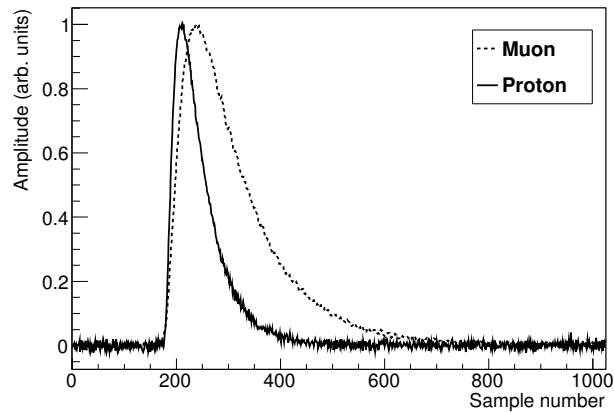


Figure 4.7: A comparison between a 70 MeV proton trace and a 70 MeV (approximately) muon trace in the lanthanum bromide. The PM-tube voltage was 900 V for the proton and 1000 V for the muon.

energy in a very small distance, just before it is stopped.

Another difference is that the muons hit the detector at an angle of 90 degrees, in comparison with the protons. This geometric difference, combined with the optical properties of the detector, could affect the pulse shapes observed.

5 Summary and outlook

5.1 Proton beam test

The phoswich array was tested with proton beam energies ranging from 70 MeV to 230 MeV. The scintillator light output was fully digitised using a sampling ADC, working at 5 GS/s, and the data was saved for off-line analysis. A DSSSD was mounted in front of the phoswich array for triggering of the setup and to obtain position data. The position data can be used to investigate what happens when protons hit a certain spot on the crystal. However, the position data has not been used in this thesis, and is left for future work.

Neither was cosmic muon data acquired during the Krakow proton beam test. Muon data would have provided a better way of comparing the detector response between muons and protons; not only to confirm the pulse shape difference, discussed in section 4.5, but also to perform an energy calibration with muons, and to correlate it with a proton energy calibration. The use of cosmic muons for the calibration of CALIFA is a natural choice. Cosmic muons are readily available in the energy range of high-energy protons. Other methods can be highly dependent on factors that are difficult to manage, such as ageing of electronic and optical components.

5.2 Pulse-shape analysis and calibration

A simple baseline calibration of the digitised scintillator light traces is presented in section 3.1, and is proven to be effective. Three methods of separating the LaBr_3 and LaCl_3 components of the trace from each other are presented in this thesis. In particular, the integral method (section 3.4) is successfully used for the proton data, and the correlation method (section 3.5) is evaluated using data from cosmic muons. The integral method is used, in combination with known proton beam energies and simulated energy loss, to perform an energy calibration (section 3.6).

The upper boundary of the trace integral is defined as a fixed point in this work. However, since the integral scales linearly with the amplitude of the pulse, an amplitude-dependent limit would be more robust; it would discard the noisy tail of low-amplitude pulses, yet include the whole tail of large-amplitude ones. Even better would be an iterative method, or neural network based algorithm, that takes into account the full pulse shape, ranging from that of pure LaBr_3 to pure LaCl_3 , and optimises the limits on a case-by-case basis.

In a BSc. thesis from 2010 [4], the energy deposited in the detector is determined by fitting a semi-empirical parametric curve to the amplitude versus I_{total} spectrum. A similar approach should be tried for the I_{tail} versus I_{total} spectrum; it could potentially provide better energy resolution, since some of the calibration error sources (section 3.6.1) then are avoided.

5.3 Data interpretation and discussion

The muon spectrum is analysed in section 4.1, and proven consistent with what can be calculated from the Bethe formula and the ratio of the scintillator light yields. The ΔE - E spectrum for protons is analysed in section 4.2, including the identification of possible nuclear reactions and detector punch-through energies. In section 4.5, the LaBr_3 scintillation is shown to be linear for

protons and for muons individually, but to have different pulse shape for protons compared with that of muons. Section 4.4 presents the energy resolution of the detector, which is found to be in the order of 3% for energies below the total punch through.

The linearity of the crystal, as considered in section 4.5, has, because of the detector geometry (figure 2.1), only been checked for protons stopped in the LaBr_3 , and for muons depositing energy in the LaBr_3 . The linearity of the LaCl_3 should be investigated in similar way. This could easily be done with muons, but to test the linearity with protons would require beam tests of a separate LaCl_3 crystal. On the other hand, the I_{total} vs. amplitude and I_{tail} vs. I_{total} plots (figures 3.2(a) and 3.2(b)) provide an indirect confirmation of the pulse shape linearity.

Futhermore, the nature of the difference in the scintillator light pulse shape for muons and proton, as described in section 4.5, has to be investigated. Ideally, muon data with the PM-voltage at 900 V should be acquired, and compared with the proton data.

Bibliography

- [1] F. J. Anscombe. The transformation of poisson, binomial and negative-binomial data. *Biometrika*, 35(3/4):pp. 246–254, 1948. 7
- [2] T. Aumann, B. Jonson, R. Lemmon, O. Tengblad, H. Scheit, H. Simon, D. Cortina, and B. Jakobsson. Technical report for the design, construction and commissioning of the califa barrel: The r3b calorimeter for in flight detection of γ -rays and high energy charged particles. Technical report, R³B collaboration, Nov 2011. 4
- [3] J. Bergström, E. Blomberg, E. Gallneby, J. Hagdahl, M. Nordström, and H. Wittler. Proton beam tests of CALIFA detector prototypes. Bachelor’s thesis, Chalmers University of Technology, 2009. 17
- [4] A. Bülling, L. Jansson, K. Jareteg, R. Masgren, G. Risting, and S. Shojaee. Analysis of CALIFA detector prototypes and silicon strip detectors. Bachelor’s thesis, Chalmers University of Technology, 2010. 33
- [5] Caen. *Mod.V1742 32+2 Ch. 12bit 5GS/s Switched-Capacitor Digitizer*, 6 edition, February 2012. Preliminary Manual. 11
- [6] David L. Donoho and Ian M. Johnstone. Ideal spatial adaptation by wavelet shrinkage. *Biometrika*, 81(3):425–455, 1994. 7
- [7] T. Aumann et al. Technical Proposal for the design, construction, commissioning and operation of R³B, A universal setup for kinematical complete measurements of Reactions with Relativistic Radioactive Beams. Technical report, GSI, 2005. 2
- [8] FAIR GmbH. *Facility for Antiproton and Ion Research*. www.fair-center.eu, Accessed: May 2013. 1
- [9] Geant 4 Collaboration. *Geant 4: A toolkit for simulation of the passage of particles through matter*. <http://geant4.cern.ch/>, Accessed: April 2013. 11
- [10] GSI Helmholtzzentrum für Schwerionenforschung GmbH. *GSI Helmholtzzentrum für Schwerionenforschung*. www.gsi.de, Accessed: May 2013. 1
- [11] H. Johansson. *ggland - command-line simulation wrapper*. <http://fy.chalmers.se/~f96hajo/ggland/>, Accessed: April 2013. 11
- [12] Kenneth S. Krane. *Introductory Nuclear Physics*. John Wiley & Sons, Inc, 2 edition, 1988. 26, 27
- [13] W. R. Leo. *Techniques for Nuclear and Particle Physics Experiments*. Springer-Verlag, 2 edition, 1994. 3, 23, 29
- [14] S. G. Mallat. *A wavelet tour of signal processing*. Academic Press, 1 edition, 1998. 6

- [15] Peter J. Mohr, Barry N. Taylor, and David B. Newell. Codata recommended values of the fundamental physical constants: 2006. *Rev. Mod. Phys.*, 80:633–730, Jun 2008. 26
- [16] J. S. Rosado. CEPA Mechanical Support. Technical report, IEM-CSIC, 2011. 11
- [17] Saint-Gobain Crystals. *BrilLanCeTM Scintillators Performance Summary*, January 2009. 16
- [18] Saint-Gobain Crystals. *BrilLanCe350 Data Sheet*, June 2012. 4, 5
- [19] Saint-Gobain Crystals. *BrilLanCe380 Data Sheet*, June 2012. 4, 5
- [20] O. Tengblad, T. Nilsson, E. Nácher, H.T. Johansson, J.A. Briz, M. Carmona-Gallardo, C. Cruz, V. Gugliemina, A. Perea, J. Sanchez del Rio, M. Turrión Nieves, J. Bergström, E. Blomberg, A. Bülling, E. Gallneby, J. Hagdahl, L. Jansson, K. Jareteg, R. Masgren, M. Nordström, G. Risting, S. Shojaee, and H. Wittler. LaBr₃(Ce):LaCl₃(Ce) Phoswich with pulse shape analysis for high energy gamma-ray and proton identification. *Nuclear Instruments and Methods in Physics Research Section A: Accelerators, Spectrometers, Detectors and Associated Equipment*, 704(0):19 – 26, 2013. 4

Glossary

- ADC** Analogue to Digital Converter. 9, 11, 15, 18, 33
- ALADiN-LAND** Setup used for kinematically complete nuclear structure experiments in Cave C at GSI. 1, 2, 4
- CALIFA** Calorimeter for in-flight emitted γ -rays and high energy charged particles. A calorimeter for use in R³B. 2, 4, 21, 33
- DAQ** data acquisition system. 9, 11, 12, 28
- DC** Direct Current. 11, 13, 15
- DSSSD** Double-Sided Silicon Strip Detector. 4, 9, 11, 12, 33
- DWT** Discrete Wavelet Transformation. 5, 6, 16
- FAIR** Facility for Antiproton and Ion Research. A new European accelerator facility being built at GSI in Darmstadt, Germany. 1
- GLAD** superconducting GSI large-acceptance dipole (GLAD). A dipole magnet that will be used to separate the reaction fragments during R³B experiments.. 2
- GS/s** Giga-Samples per second. 9, 11, 18, 33
- GSI** Gesellschaft für Schwerionenforschung. An accelerator facility for heavy ion research, located in Darmstadt, Germany. 1
- Hygroscopicity** The property of attracting and holding water from the environment. 3, 4
- LAAPD** Large area avalanche photo diode. A light read-out device used in some scintillator detectors. 4
- NeuLAND** The New Large Area Neutron Detector in the R³B setup.. 2
- NUSTAR** Nuclear Structure, Astrophysics, and Reactions. An experimental program at FAIR. 1
- Phoswich** A type of scintillator detector composed of two optically coupled scintillator materials that have a single read-out device. 4, 11, 28
- PM** A light read-out device commonly used in scintillator detectors. 3–5, 7, 9, 17, 18, 29, 34
- PSA** PSA refers to various methods of analysing pulse shapes, e.g. from scintillators, to extract physical information. 4, 5

PSD PSD refers to various methods of discriminating particle species of hits in a detector. 3, 29

QE Quantum Efficiency. 3

Quenching Radiationless de-excitations, or fully occupied electronic states, introducing energy “losses” in a scintillator material. 3

R³B An international collaboration aiming to study reactions with relativistic radioactive beams. The abbreviation also refers to the experimental setup itself. 1, 2, 4

Super-FRS A high-resolution in-flight separator for exotic nuclei. 1

TF Fast amplifier used for timing applications. 9

VME VERSAmodule Eurocard bus. Commonly used bus standard in physics and industry. 11

XB Scintillator detector surrounding the target chamber at the ALADiN-LAND setup. 4

A Table of energy resolution

Energy (MeV)	Energy resolution (%)				
	Crystal 1	Crystal 2	Crystal 3	Crystal 4	Crystal 5
61.0	4.54 ± 0.04	4.53 ± 0.03	4.75 ± 0.03	4.64 ± 0.03	5.36 ± 0.04
72.0	3.82 ± 0.02	3.80 ± 0.02	3.98 ± 0.02	4.16 ± 0.02	4.62 ± 0.02
82.8	3.42 ± 0.02	3.34 ± 0.02	3.47 ± 0.02	3.61 ± 0.02	3.91 ± 0.02
93.4	3.13 ± 0.02	3.03 ± 0.02	3.16 ± 0.02	3.31 ± 0.02	3.50 ± 0.01
103.8	2.87 ± 0.02	2.78 ± 0.02	2.84 ± 0.02	3.04 ± 0.02	3.15 ± 0.01
114.2	2.67 ± 0.00	2.50 ± 0.02	2.65 ± 0.02	2.78 ± 0.02	4.96 ± 0.02
124.5	2.49 ± 0.03	2.39 ± 0.02	2.43 ± 0.02	2.58 ± 0.02	3.86 ± 0.01
134.8	3.56 ± 0.10	3.20 ± 0.11	3.88 ± 0.12	4.01 ± 0.06	—
145.0	3.85 ± 0.04	3.82 ± 0.03	3.62 ± 0.03	3.49 ± 0.05	3.51 ± 0.02
155.3	2.72 ± 0.06	2.48 ± 0.06	2.51 ± 0.05	2.76 ± 0.05	3.11 ± 0.05
165.5	2.78 ± 0.06	2.14 ± 0.05	2.49 ± 0.04	2.69 ± 0.05	3.20 ± 0.06
175.6	4.10 ± 0.04	3.14 ± 0.03	2.49 ± 0.03	2.60 ± 0.03	4.09 ± 0.04
216.0	8.92 ± 0.19	6.47 ± 0.16	7.04 ± 0.14	6.97 ± 0.13	11.47 ± 0.10

Table A.1: Energy resolution for the five $\text{LaBr}_3:\text{LaCl}_3$ phoswich crystals for selected proton energies. Crystals 1 to 4 are the four crystals of the phoswich array, while crystal 5 is the shorter cylindrical crystal. The error bars are the propagated 1σ error bars of the fit.

B Table of multiplicity, coincidence, and add-back gain

Energy (MeV)	Gain (%)	Multiplicity (%)			
		1	2	3	4
70	100.4 ± 0.8	99.56 ± 0.78	0.44 ± 0.03	0.00 ± 0.00	0.00 ± 0.00
80	100.9 ± 0.5	99.08 ± 0.54	0.92 ± 0.03	0.00 ± 0.00	0.00 ± 0.00
90	101.6 ± 0.6	98.35 ± 0.60	1.65 ± 0.04	0.01 ± 0.00	0.00 ± 0.00
100	102.2 ± 0.6	97.77 ± 0.60	2.23 ± 0.05	0.00 ± 0.00	0.00 ± 0.00
110	102.2 ± 0.7	97.79 ± 0.66	2.21 ± 0.06	0.01 ± 0.00	0.00 ± 0.00
120	102.2 ± 0.9	97.81 ± 0.82	2.17 ± 0.07	0.02 ± 0.01	0.00 ± 0.00
130	101.1 ± 0.9	98.81 ± 0.90	1.19 ± 0.06	0.00 ± 0.00	0.00 ± 0.00
140	103.2 ± 3.5	96.75 ± 3.30	3.20 ± 0.36	0.06 ± 0.04	0.00 ± 0.00
150	104.6 ± 1.3	95.46 ± 1.20	4.51 ± 0.16	0.03 ± 0.01	0.00 ± 0.00
160	107.4 ± 3.1	93.03 ± 2.70	6.93 ± 0.47	0.04 ± 0.03	0.00 ± 0.00
170	108.9 ± 3.3	91.78 ± 2.79	8.20 ± 0.55	0.02 ± 0.02	0.00 ± 0.00
180	110.5 ± 1.8	90.43 ± 1.48	9.46 ± 0.32	0.11 ± 0.03	0.00 ± 0.00
220	121.4 ± 3.1	78.80 ± 2.04	20.40 ± 0.80	0.80 ± 0.12	0.00 ± 0.00

Table B.1: The table first lists the gain of using add-back for fully stopped protons—or punch through protons, in the case of 220 MeV protons—expressed in percentage of same type of protons without using add-back. A crystal is considered to have triggered when the maximum pulse amplitude is above 30 ADC channels; 10 channels above the maximum observed noise. The error is the propagated 1σ intrinsic statistical error of the count numbers.

Energy (MeV)	Coincident crystal pair (%)					
	1-2	1-3	1-4	2-3	2-4	3-4
70	5.2 ± 1.7	0.7 ± 0.5	18.1 ± 3.6	55.7 ± 7.7	0.7 ± 0.5	21.6 ± 4.0
80	5.5 ± 0.8	0.4 ± 0.2	30.9 ± 2.5	42.9 ± 3.1	0.3 ± 0.2	20.2 ± 1.8
90	6.7 ± 0.8	0.7 ± 0.2	29.7 ± 2.0	42.1 ± 2.5	0.6 ± 0.2	21.1 ± 1.6
100	6.4 ± 0.7	0.5 ± 0.1	31.9 ± 1.8	38.9 ± 2.1	0.6 ± 0.2	22.1 ± 1.4
110	6.7 ± 0.7	0.7 ± 0.2	30.5 ± 1.9	42.4 ± 2.4	0.6 ± 0.2	19.6 ± 1.4
120	7.5 ± 1.0	0.5 ± 0.2	31.5 ± 2.5	44.5 ± 3.1	1.1 ± 0.3	16.7 ± 1.6
130	5.6 ± 1.2	0.7 ± 0.4	35.3 ± 4.0	48.5 ± 4.9	0.9 ± 0.4	9.4 ± 1.7
140	0.9 ± 1.0	1.8 ± 1.4	57.9 ± 12.5	21.1 ± 6.3	0.9 ± 1.0	21.1 ± 6.3
150	8.7 ± 1.1	0.8 ± 0.3	33.1 ± 2.7	40.1 ± 3.0	0.7 ± 0.3	17.8 ± 1.8
160	12.0 ± 2.5	1.2 ± 0.6	32.9 ± 4.9	36.7 ± 5.3	0.6 ± 0.4	17.8 ± 3.2
170	12.7 ± 2.5	0.8 ± 0.5	34.0 ± 4.8	36.4 ± 5.0	1.3 ± 0.7	15.4 ± 2.8
180	12.1 ± 1.2	0.7 ± 0.2	31.7 ± 2.3	39.4 ± 2.6	1.3 ± 0.3	17.1 ± 1.5
220	9.7 ± 1.1	2.6 ± 0.5	45.3 ± 3.0	38.2 ± 2.6	2.9 ± 0.5	8.7 ± 1.0
Mean	6.77 ± 0.08	0.62 ± 0.01	31.85 ± 0.55	40.61 ± 0.75	0.63 ± 0.01	16.12 ± 0.22

Table B.2: The coincidence between crystals for fully stopped protons—or punch through protons, in the case of 220 MeV protons—expressed as a percentage of the total number of coincidence events for those protons. The weighted mean is also given. A crystal is considered to have triggered when the maximum pulse amplitude is above 30 ADC channels; 10 channels above the maximum observed noise. The error is the propagated 1σ intrinsic statistical error of the count numbers. Refer to figure 2.1 for the labelling of crystals.

C Table of calibration parameters

Table C.1 shows the pulse separation and energy calibration parameters used in the following calibration:

$$\begin{cases} \Delta E_{\text{Br}} = b_0 + b_1 I_{\text{total,Br}} = b_0 + b_1 \frac{I_{\text{tail}} - a_{\text{Cl}} I_{\text{total}}}{a_{\text{Br}} - a_{\text{Cl}}} \\ \Delta E_{\text{Cl}} = b_2 + b_3 I_{\text{total,Cl}} = b_2 + b_3 \frac{a_{\text{Br}} I_{\text{total}} - I_{\text{tail}}}{a_{\text{Br}} - a_{\text{Cl}}} \end{cases}.$$

The parameters are applicable for the data acquired during the Krakow beam tests. See sections 3.4 and 3.6 for details.

Parameter	Crystal 1	Crystal 2	Crystal 3	Crystal 4	Crystal 5
a_{Br}	1.0699×10^{-1}	1.0706×10^{-1}	1.0551×10^{-1}	1.0888×10^{-1}	1.0201×10^{-1}
a_{Cl}	2.6020×10^{-1}	2.5981×10^{-1}	2.5361×10^{-1}	2.5683×10^{-1}	2.4592×10^{-1}
b_0	3.2305	2.3421	4.4473	4.4710	6.2646
b_1	1.0438×10^{-3}	8.6610×10^{-4}	9.3792×10^{-4}	1.2505×10^{-3}	1.3092×10^{-3}
b_2	-2.3028	-3.5859×10^{-1}	-2.8687×10^{-1}	-2.0041	-6.258
b_3	2.4246×10^{-3}	1.9228×10^{-3}	2.0183×10^{-3}	2.7962×10^{-3}	3.3644×10^{-3}

Table C.1: Pulse separation and energy calibration parameters for the five $\text{LaBr}_3:\text{LaCl}_3$ phoswich crystals. Crystals 1 to 4 are the four crystals of the phoswich array, while crystal 5 is the shorter cylindrical crystal.